Research article

PG
Petroleum Geoscience

https://doi.org/10.1144/petgeo2021-065 | Vol. 28 | 2022 | petgeo2021-065

Petrographic and diagenetic investigation of the distal Triassic 'Budleighensis' fluvial system in the Solway and Carlisle Basins for potential CO_2 storage

J. R. Marsh[1]*, S. J. Jones[1], N. S. Meadows[2] and J. G. Gluyas[3]

[1] Department of Earth Sciences, Durham University, Durham DH1 3LE, UK
[2] Redrock International Ltd, 38 Queens Drive, Prenton, Wirral CH43 0RP, UK
[3] Durham Energy Institute, Durham University, Durham, County Durham DH1 3LE, UK
JRM, 0000-0002-7360-6762
* Correspondence: joshua.marsh@durham.ac.uk

Abstract: Failure to find hydrocarbon prospects in the Solway Basin region has resulted in a lack of research into the local Sherwood Sandstone Group petrography, reservoir quality and depositional history compared to the analogous southern reservoirs in the EISB which will be utilized for carbon storage. A detailed petrographic study is presented which aims to understand if the Solway Firth could have similar utility. The Permo–Triassic Sherwood Sandstone Group is believed to be deposited in depocentres connected during the Early Triassic by the extensive 'Budleighensis' fluvial system. Here, the Solway and Carlisle basins are proposed as terminal sites for this endorheic system, with the Lower Triassic Annan Sandstone Formation ascribed to the distal region of a fluvial distributary zone and the overlying Kirklinton Sandstone Formation thought to mark a transition to a basinal zone, depositing aeolian sandstones and locally associated playa lake facies. Fluid inclusion, stable isotope burial history modelling and field observations have been used to assess the relative timing and importance of different diagenetic cements. Early diagenetic cements include grain-rimming haematite and patchy calcite cement, especially in the Annan Sandstone Formation. Later burial diagenesis sees further calcite cement, quartz overgrowths and, restricted to the Kirklinton Sandstone Formation, ferroan dolomite. Porosity and permeability show significant differences between fluvial Annan and aeolian Kirklinton facies associations. Despite the finer grain size, a reservoir with excellent porosity and permeability as well as no hydrocarbon charging or legacy hydrocarbon extraction is persevered, suggesting the Solway Basin could be a secure CO_2 storage site.

Supplementary material: An overview of the primary and secondary data collected and utilised in this study, as well as raw data values are available at https://doi.org/10.6084/m9.figshare.c.5906677

This article is part of the Energy Geoscience Series available at https://www.lyellcollection.org/cc/energy-geoscience-series

Received 13 August 2021; **revised** 18 January 2022; **accepted** 19 March 2022

The offshore and onshore NW England Triassic succession, comprising Early–Middle Triassic (Olenekian–Ansian) Sherwood Sandstone Group (SSG), and the Middle–Late Triassic (Anisian–Norian) Mercia Mudstone Group (MMG), represents part of a large-scale internal drainage system in the semi-arid to arid interior of the Pangaea supercontinent. NW Europe lay between 15°N and 25°N and was influenced by SW-directed subtropical trade winds giving rise to general semi-arid to arid conditions with an annual summer monsoon and intense seasonality (Kutzbach and Gallimore 1989; Parrish 1993; Szulc 1999; Preto *et al.* 2010).

The Middle Triassic sediments infilled extensional rift basins with Early Triassic fill ascribed to the action of a major northward flowing river system, first termed the 'Budleighensis' fluvial system by Wills (1951). This system carried material from the Variscan massifs of western and central Europe in >400 km northwards through the Wessex, Worcester, Stafford and Cheshire Basins of England, exiting into the East Irish Sea Basin (EISB) where it formed a sand-dominated, lower flow regime, low to moderate sinuosity braided river system (Fig. 1; Audley-Charles 1970; Warrington and Ivimey-Cooke 1992; Hounslow and Ruffell 2006; Tyrrell *et al.* 2012; Ambrose *et al.* 2014).

Within the arid Pangean climate, aeolian-derived facies are preserved amongst fluvial deposition, increasing northwards and becoming dominant at basin margins such as at Sellafield, West Cumbria (Jones and Ambrose 1994; Hounslow and Ruffell 2006). The reservoir properties and depositional framework of the SSG within the EISB has been extensively researched due to the region's abundance of hydrocarbon-prolific wells (Meadows and Beach 1993*a*, *b*; Meadows 2006). The EISB extends offshore from Liverpool Bay and the north coast of Wales northwards to Ramsey–Whitehaven Ridge, located between the west Cumbrian coast and the east coast of the Isle of Man, where it borders the Solway Basin to the north (Fig. 1). Failure of hydrocarbon exploration within the Solway Basin has meant little investigation has been conducted into its reservoir system, which is analogous to the proven hydrocarbon systems within the EISB, since the late 1990s (e.g. Newman 1999). As a consequence, the sandstone petrography of the Lower–Middle Triassic of the Solway Basin and its relation to the Budleighensis fluvial system is comparatively less well understood than that of the proximal EISB (Fig. 1; Akhurst *et al.* 1997; Meadows 2006; Tyrrell *et al.* 2012). It has been suggested that the Triassic sandstones deposited in the Solway Basin were isolated from the EISB by the Ramsey–Whitehaven Ridge; a NE–SW trending fault-bounded high throughout much of the Late Paleozoic and Mesozoic Era (Newman 1999; Quirk *et al.* 1999; Floodpage *et al.* 2001). Alternatively, Meadows (2006) suggests that the Budleighensis system diverted westwards into the Peel Basin, whilst Hounslow and Ruffell (2006) suggest that the system may have terminated in the Solway Basin or, which they deem more likely, diverted northwards into the proto-Atlantic.

In this study we attempt to characterize the distal section of the 'Budleighensis' fluvial system spatially and temporally during the

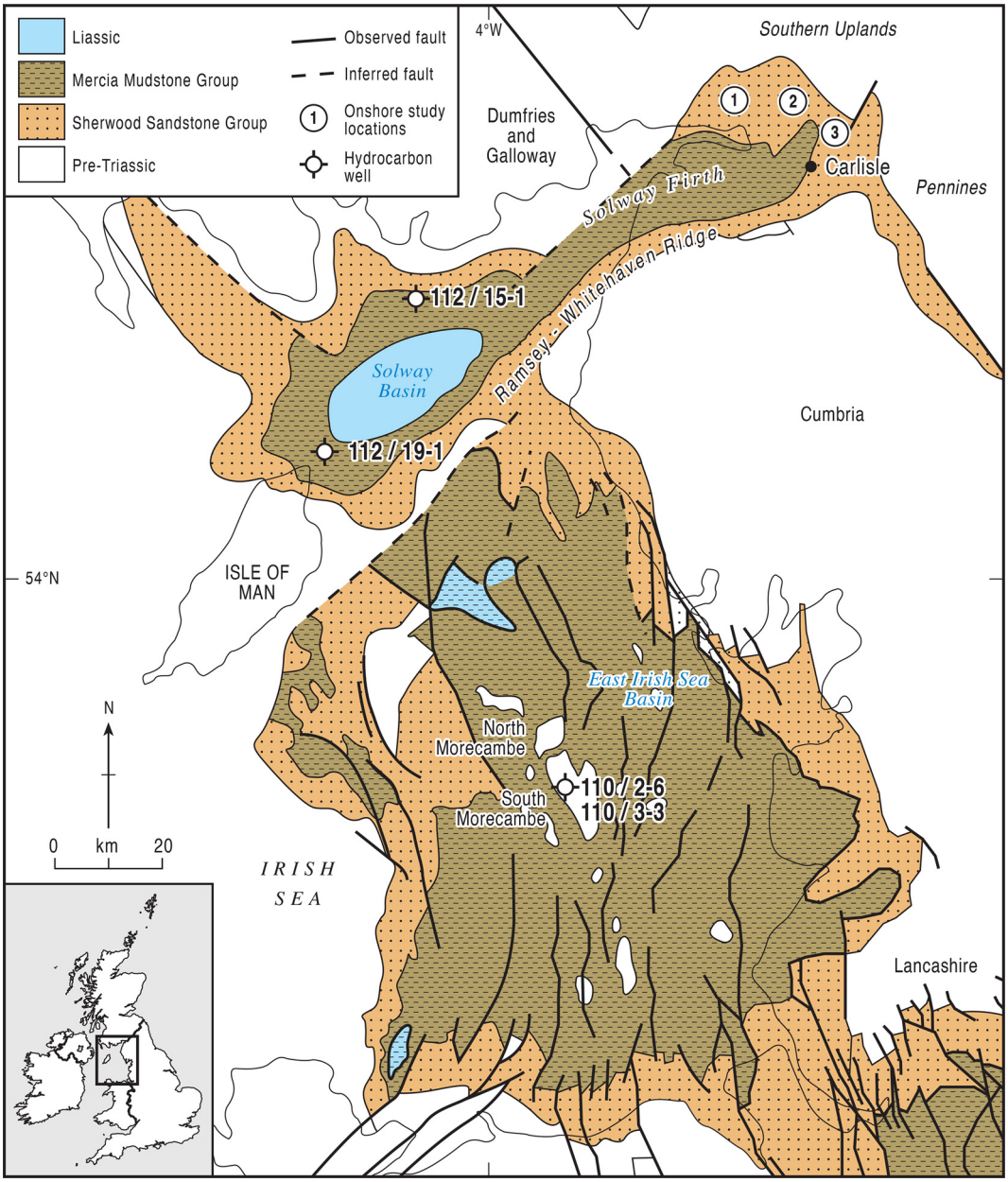

Fig. 1. Location map of the Solway, Carlisle and East Irish Sea Basins (EISB). Onshore field study locations, well 110/2-6 and 111/3-3 in the EISB and 112/15-1 and 112/19-1 in the Solway Basin are identified. Location (1) Lower Annan Sandstones, Cove Quarry [NY 254 710]; (2) Upper Annan Sandstones, Glinger Burn gorge [NY 376 725]. (3) Kirklinton Sandstones, Cliff Bridge, [NY 4136 6619]. Geological structure generalized from Jackson *et al.* (1995); Chadwick (1997) and Newman (1999).

deposition of the Early–Middle Triassic Annan and Kirklinton Sandstone Formations of the Solway Basin SSG, interpreting the nature of its termination. We present new results for the petrography and diagenesis of these sandstones, supported by offshore hydrocarbon data within the Solway Basin. Offshore hydrocarbon data from contemporaneous aged hydrocarbon reservoirs in the North and South Morecambe Fields of the EISB are additionally used to compare the porosity, permeability and petrography of the Solway Basin to its southern counterpart. This comparison will allow the porosity and permeability of the Solway Basin reservoir to be compared to benchmark proven hydrocarbon reservoirs and utilize any differences in petrography to determine the Solway Basin's depositional position in the overall Budleighensis system. The approach presented in this paper provides an important step towards identifying the distribution of facies, better understanding of this significant drainage system, its termination, and the effect this has had on the less-well constrained petrography and reservoir characteristics of the Solway and Carlisle Basins. Once better constrained, the utility of this reservoir system as a potential CO_2-storage site is explored. Analogous reservoir systems in the EISB have already been chosen as carbon storage sites for the Hynet North West Project, a decarbonized industrial cluster project that will see simultaneous carbon capture and storage (CCS), utilizing Liverpool Bay depleted oil and gas reservoirs, and hydrogen production (HyNet 2021). This project is backed by the UK Government as one of two Track-1 projects, which will mean decarbonization will begin by 2025 and will both have access to £1 billion of state-funding (GOV.UK 2021).

The Solway Basin

Geological setting

The western side of England and Southern Scotland was subject to extensive faulting during the Permo–Triassic period and was concentrated in a roughly north–south trend from SW England to

the Solway Firth, forming the large depocentres that would form the pathway to the 'Budleighensis' fluvial system and be filled by the SSG. This system would flow through a tectonically controlled landscape of topographically high massifs and deep pocket-like basins, with inter-massif channels connecting them (Newell 2018).

Such Permo–Triassic basins within Britain and NW Europe developed in response to east–west extension associated with the post-Variscan break-up of Pangaea and periodic rifting in the North Atlantic (Jackson and Mulholland 1993; Newman 1999; McKie and Williams 2009). The structural boundaries of these basins are formed by NE–SW trending thrusts and NW–SE trending transfer faults inherited from the Caledonian and Variscan Orogenies (Newman 1999). This strong control of Caledonian and Variscan structures upon the development of these basins is reflected in their present-day orientation, whereby the Carlisle, Solway and Peel Basins have a broad NE trend, whereas other nearby Permo–Triassic basins such as the Vale of Eden and EISB, have a marked NNW orientation (Fig. 1; Jackson and Mulholland 1993; Chadwick *et al.* 1995, 2001; Akhurst *et al.* 1997; Holliday *et al.* 2004).

Both the Solway Basin and its onshore extension, the Carlisle Basin, have undergone a complex tectono-stratigraphic evolution, involving several phases of extension and basin development followed by periods of uplift and erosion. Both basins crosscut structures of the underlying early Permian rift basins (Newman 1999; Floodpage *et al.* 2001; McKie and Williams 2009) and predates the late Triassic–Jurassic rifting phase, which began with the opening of the Central Atlantic Ocean (Manspeizer 1988). The late Permian to Jurassic sequences were deposited in response to regional post-rift thermal relaxation, which was initiated in the Early Carboniferous, forming an intracontinental basin 30–50 km wide and 125 km long (Quirk and Kimbell 1997; Newman 1999). In the basin centre, the fill comprises over 1600 m of Lower–Middle Triassic strata (Sherwood Sandstone Group) and interpreted to have been deposited in a variety of arid to hyperarid continental environments, differing from the general semi-arid to arid conditions of NW Europe (Brookfield 2004, 2008). Regional subsidence continued in the Late Triassic with the deposition of a thick succession of evaporates and shales which have been assigned to the MMG in the Solway Basin and laterally the Stanwix Shale in the Carlisle Basin (Fig. 2).

It is widely accepted that significant syn-depositional faulting and extension took place during the deposition of the SSG of the Lower–Middle Triassic within the EISB, as seen in seismic reflection data (Jackson and Johnson 1996; Chadwick *et al.* 2001), extension modelling (Rowley and White 1998) and facies distribution mapping (Meadows and Beach 1993*a*, *b*). This extension was broadly orientated east–west throughout much of the Triassic (Chadwick and Evans 1995; Jackson *et al.* 1995). In addition, Meadows and Beach (1993*a*) identify that basin evolution not only controlled facies distribution and depositional environment but this cumulatively influenced the distribution of grain populations. Grain size, which reservoir quality within the EISB has ultimately depended, is dependent on facies type (aeolian v. fluvial) and location along the fluvial system.

Despite evidence for a correlation between active Triassic faulting and facies development within the EISB, this does not seem to be the case in the Solway and Carlisle Basins. The SSG of the Solway Basin records a relatively uniform succession of fluvial and aeolian facies where uniform stratigraphic thicknesses are maintained across the Basin, including basin margins (Fig. 1; Chadwick *et al.* 1995; Jackson *et al.* 1995; Akhurst *et al.* 1997; Quirk and Kimbell l997; Newman 1999; Floodpage *et al.* 2001; Brookfield 2008).

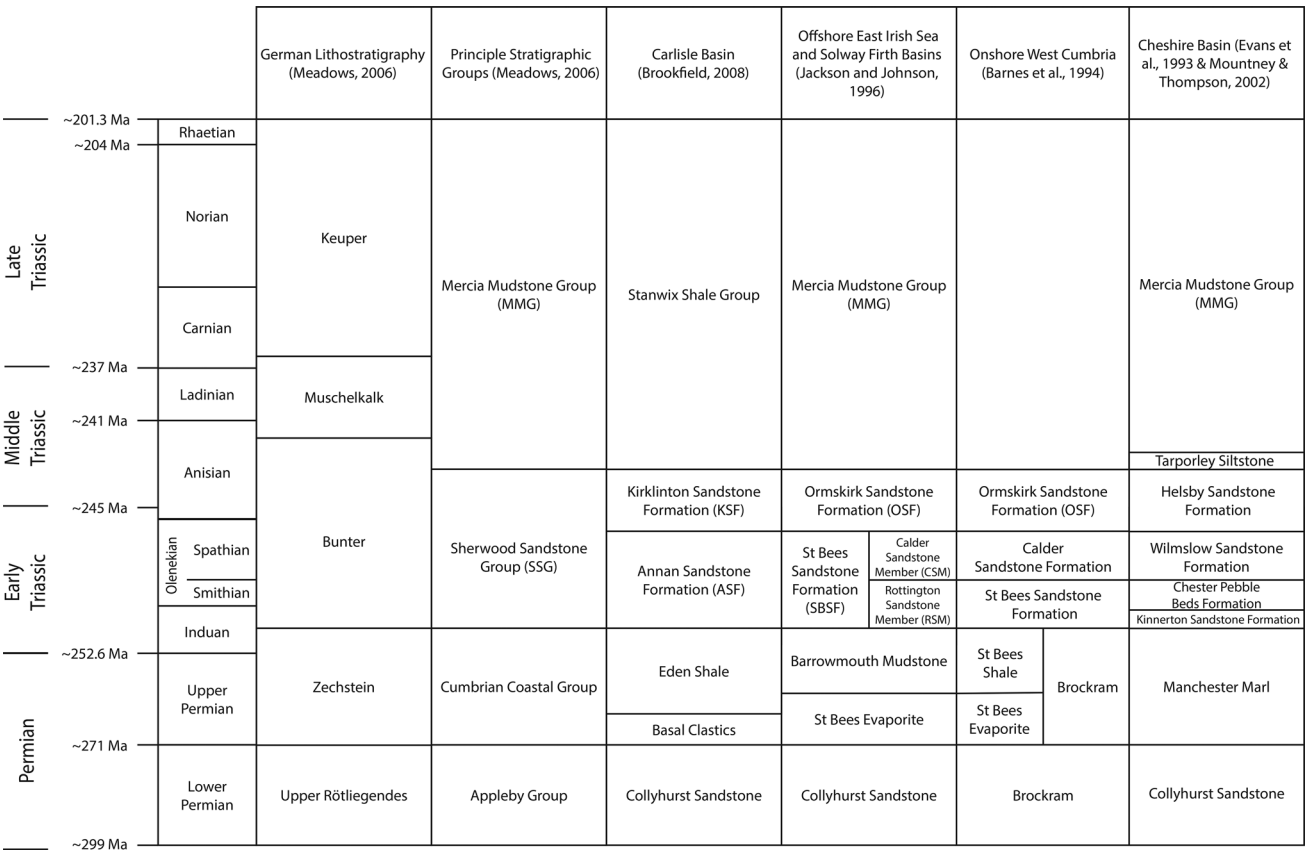

Fig. 2. General stratigraphy for the Permo–Triassic of the Solway Basin and its relationship to surrounding basins. Major groups and biostratigraphy dates based on work by Brookfield (2008); Newell (2018); Hounslow and Ruffell (2006) and Meadows (2006). Stratigraphy and nomenclature based on Meadows (2006); Brookfield (2008); Jackson and Johnson (1996); Barnes *et al.* (1994); Evans *et al.* (1993) and Mountney and Thompson (2002).

Stratigraphy

The Permo–Triassic red bed succession lies unconformably upon all underlying units and structures. The Cumbrian Coastal Group is up to 190 m thick in boreholes within the Solway Basin and begins with a very thin (10 m) and variable breccia unit, known as the Basal Clastics (Fig. 2). Where the Basal Clastics overlie Carboniferous rocks, clasts in the basal strata are locally derived and have been interpreted to have accumulated in small fans around low hills and knolls (e.g. Holliday *et al.* 2004). A relatively thick (180 m) gypsum/anhydrite evaporite and red shale unit overlies this breccia, known as the Eden Shales. This unit is a direct correlative of the St Bees Shale and St Bees Evaporite of the EISB and West Cumbria (Brookfield 2008). However, solution removal of evaporites at the surface means only the upper clastic part is exposed at outcrop within the Solway Basin.

The Eden Shales sit below the fine-grained sandstones of the SSG (Fig. 2), which is the focus of this study and has a maximum recorded thickness of *c.* 1248 m offshore in well 112/15-1. The SSG comprises two distinct facies: the Annan Sandstone Formation (hereby ASF) and Kirklinton Sandstone Formation (hereby KSF). The lower junction of the ASF is transitional from the Eden Shales and this facies consists of mainly thick (*c.* 2 m) bedded multi-channel stacked sandstones, with relatively thick interbedded siltstone and mudstone units. The upper part of the ASF again consists of multi-storey channel units, but which reach up to 10 m thick and feature only thin mudstone and siltstone interbeds (Brookfield 2004). Facies associations within the ASF include flood plain fines and playa sediments, which are common features throughout, forming in association with both ribbon and sheetflood fluvial sandstones. The KSF sharply overlies the ASF, marking a sharp contrast in depositional style from stacked fluvial channels below to aeolian deposition above (Brookfield 2004, 2008). Specifically, onshore the KSF features dominantly dry facies, characteristically in the form of large (up to 2 m) cross beds with swept-out toesets as part of aeolian dune structures. Subordinate wet/damp facies with damp interdune and damp sandflat features are also present. Similar depositional facies to those described above are recognized within the correlative units of the EISB (Cowan 1993; Meadows and Beach 1993*a*, *b*; Meadows 2006).

The principal reservoir sequence within the EISB is formed by the upper St Bees Sandstone Formation (hereby SBSF) of the SSG and the overlying Ormskirk Sandstone Formation (hereby OSF) (Fig. 2; Meadows and Beach 1993*b*). These units are direct equivalents of the upper ASF and KSF within the Solway Basin, respectively (Fig. 2). The SBSF in the EISB was divided into the lower Rottington Sandstone Member (hereby RSM) (*c.* 550 m) and upper Calder Sandstone Member (hereby CSM) (*c.* 650 m) by Colter and Barr (1975) and Jackson *et al.* (1987), citing a shift in the geophysical log profile and creating the 'Top Silicified Zone' boundary between the two. The base of the OSF in the EISB is identified by a seismic marker thought to relate to the regional Hardegsen Disconformity (Barnes *et al.* 1994).

The KSF is overlain by the Stanwix Shales; the equivalent of the MMG of the EISB (Fig. 2). This unit comprises a thick succession of shales with evaporites, proven up to *c.* 813 m thick in the Solway Basin (well 112/15-1) and up to 3700 m in the EISB (Wilson 1990). The presence of halite beds within the MMG is critical to seal efficiency because of the multiple periods of fault reactivation during the Early Cretaceous (Late Cimmerian phase) and Tertiary (Floodpage *et al.* 2001).

Petrographic methods and data collected

Primary data collection for this study consisted of the extraction of onshore hand specimen samples from three exposures of the Lower and Upper ASF and the KSF, of the Solway and Carlisle Basins. These sections were chosen as the most well exposed, representative locations of the formations, where samples were collected on exposed surfaces by hammer and chisel (Brookfield 2004, 2008). Thirty-four samples of the Lower ASF were taken from Cove Quarry (Fig. 1, Location 1; Figs 3a and 4), six samples of the Upper ASF were taken from the gorge of the River Lyne at Glinger Burn (Fig. 1, Location 2; Fig. 4) and sixteen samples of the KSF were taken from the Cliff Bridge section (Fig. 1, Location 3; Fig. 3b). In each case, samples were taken at 0.5 m intervals to allow accurate, detailed documentation of the vertical change in facies and petrography. These samples were prepared into 76 mm by 26 mm blue epoxy-impregnated thin sections, revealing porosity. Where possible thin sections were cut perpendicular to bedding/lamination. As field samples, weathering could have influenced porosity and permeability, however samples were chosen with no weathering rind or from the immediate surface of the exposure to mitigate this effect.

Mineral composition, including authigenic minerals and cements, was determined using point-counting thin section micrographs on a PETROG stepping-stage and counting software under a Leica DM2500P microscope with 300 counts per sample. This data was used for QLF classification. Optical porosity was measured by using the digital image analysis technique, jPOR (Grove and Jerram 2011). The programme jPOR is a macro file (jPOR.txt), which is utilized within the Java-based image manipulation programme, ImageJ (Abramoff *et al.* 2004). By using jPOR, total optical porosity was determined in a short space of time and provided comparable results to more time-consuming point counting, but with significantly less 'counting error' and less variability than published point counting studies (Grove and Jerram 2011). For the measurement of permeability, a portable hand-held mechanical Tiny-perm II Air mini Permeameter was used for rapid in-situ determination of permeability at outcrop and on fresh hand specimens with >120 measurements taken (Chandler *et al.* 1989). Samples were collected in the field and then analysed in the laboratory on flat sections and where a good seal could not be achieved a new flat cut section was produced.

Petrography (including porosity) was used to calculate compactional and cementational porosity loss using the methodologies 'Calculation of Compactional Porosity Loss (COPL)' and 'Cementational Porosity Loss (CEPL)' outlined by Houseknecht (1987) and further explained by Stricker *et al.* (2016).

All thin sections (n:56) were then highly polished to 30 µm and coated with carbon prior to analysis by a Hitachi TM 1000 scanning electron microscope (SEM) and a Hitachi SU-70 field emission gun (FEG), both equipped with an energy dispersive detector (EDS). SEM analyses of thin section and bulk rock samples were conducted at 15–20 kV acceleration voltage with beam currents of 1 and 0.6 nA, respectively. Point analyses had an average duration of 2 minutes, whereas line analyses were dependent on length. SEM-EDS was used for rapid identification of chemical species. Constituents such as small macroquartz and porous clay fill were identified and quantified using a mixture of SEM and SEM-CL.

Oxygen and carbon isotope analysis was then conducted using the primary petrography samples. Calcite and ferroan dolomite cements were analysed from the ASF (n:23) and KSF (n:17), respectively, where samples were ground and reacted with phosphoric acid and the evolved gas for each carbonate fraction was analysed using a ThermoScientific MAT 253 mass spectrometer. Precision was monitored and was better than 0.1‰ PDB for both $\delta^{13}C$ and $\delta^{18}O$.

Microthermometric fluid inclusion analysis of the ASF (n:10) from Cove Quarry and KSF (n:4) from Bridge Cliff was carried out using double polished wafers for conditions of cementation and formation waters, where quartz overgrowths and both quartz

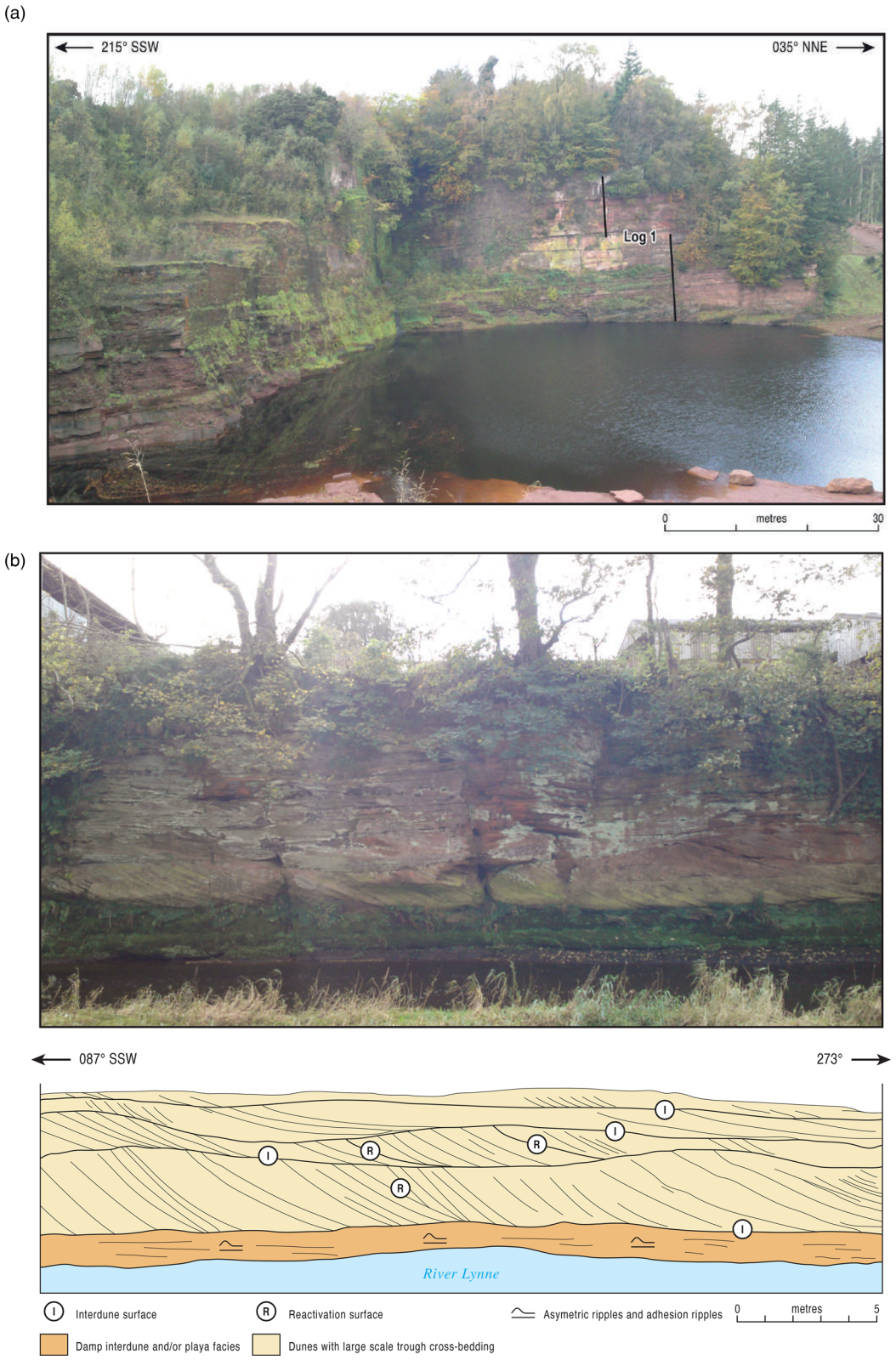

Fig. 3. (**a**) Cove Quarry section [NY 254 710], showing the Lower ASF with stacked sheet-like fluvial sandstones at the base and progressively developing more erosional bases and ribbon like channel geometries. Location of Log 1 and hand-specimen sample sites identified: see Figure 4 for detailed graphic log and Table 1 for sample details, (**b**) aeolian dune trough cross-bedding and interdune playa facies of the KSF at River Lyne Section, Cliff bridge [NY 4136 6619].

overgrowths and dolomite cements were sampled from each Formation, respectively. Analysis was conducted on a Linkam THM600/TS90 motorised X and Y, heating and cooling stage linked to a Leica DM2500P polarizing microscope. Accuracy and control over the temperature range of −196 to 600°C enables fluid inclusions to be characterized to better than ±0.1°C, over the range of temperatures reported here. Routinely available measurements are homogenization temperatures (T_h) and final melting temperatures (T_m). Homogenization is the conversion of multiphase inclusion contents to a single phase (usually at temperatures

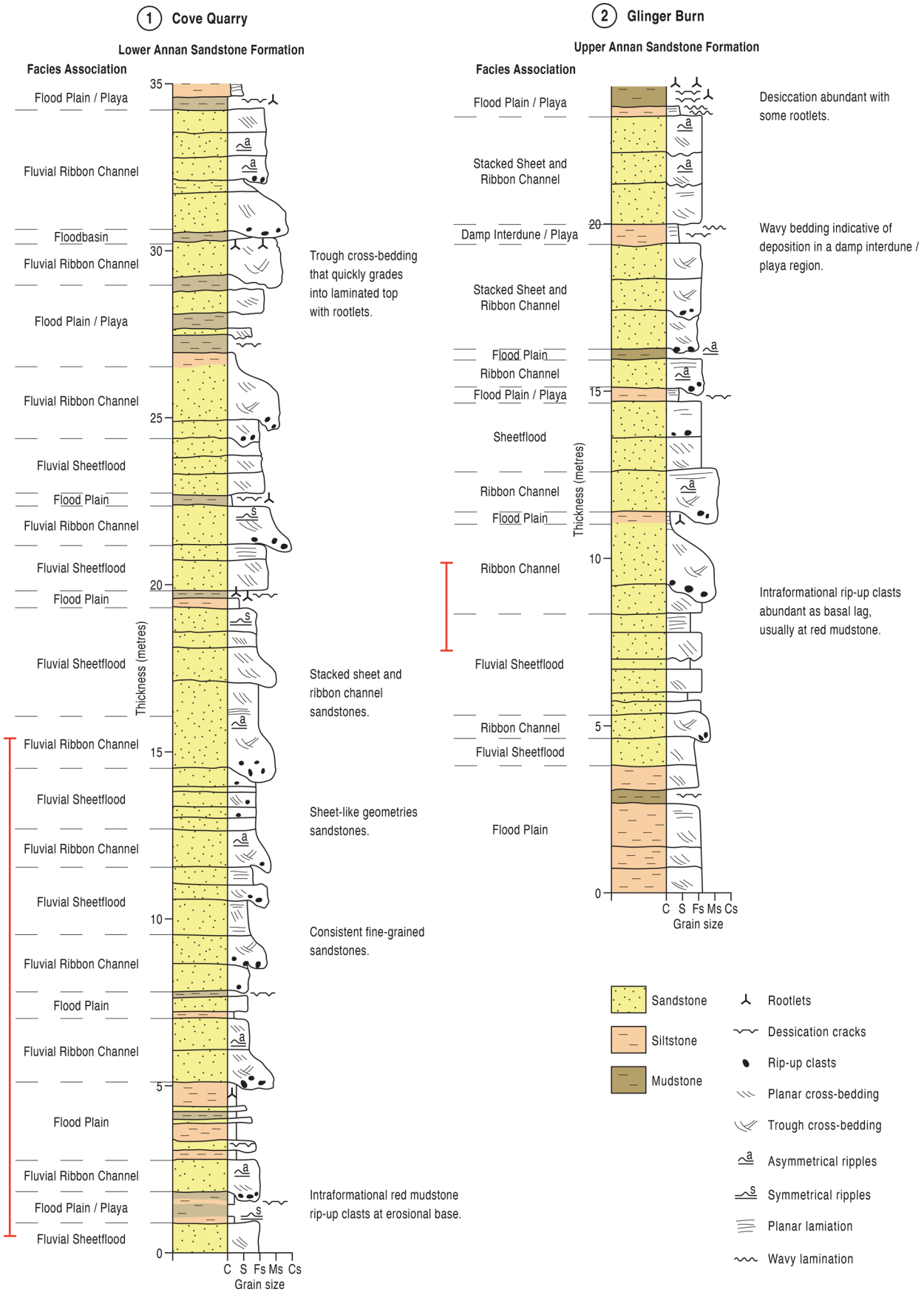

Fig. 4. Graphic logs of the Lower ASF at Cove Quarry and Upper ASF at Glinger Burn. Facies associations are identified. See Figure 1 for site locations. Collected sample sites are identified by the red line (see Table 1).

above room temperature). Interpreting homogenization temperatures in carbonates, sulfates and halides can be complicated because aqueous inclusions can reset to higher temperature if they are overheated beyond a threshold which is dependent on the mineral strength and inclusion geometry (Goldstein and Reynolds 1994; Goldstein 2001). This can occur in the laboratory as well as through

Table 1. *Modal petrographic point counting data for onshore Solway Firth Samples collected from Cove Quarry (Lower ASF), Glinger Burn (Upper ASF) and Bridge Cliff (KSF) (See Figs 1, 3a, b and 4)*

Sample location/ height	Detrital mineralogy						(Authigenic) blocky cement			Authigenic clay					Porosity	Facies association*
Lower Annan	Total qtz	Total fspr	Meta lith	Ig lith	Total mica	Smectite/mixed clay	Total blocky cem	Calcite	Quartz	Fe dolomite	Haematite	Total clay cem	Illite/mixed layer I/S	Kaolinite		
1/ 0 m	62.2	4.2	7.1	5.2	2.1	0.5	1.0	0.0	1.0	0.0	0.0	3.3	3.3	0.0	15.2	Fluvial Sheetflood
2/ 0.5 m	61.5	7.2	2.7	6.5	0.8	1.0	1.7	0.0	1.7	0.0	0.0	2.3	2.3	Tr	16.7	Fluvial Sheetflood
3/ 1 m	63.6	5.5	1.8	4.5	1.0	0.5	10.1	6.8	3.3	0.0	0.0	3.8	3.3	0.5	11.0	Fluvial Sheetflood
4/ 1.5 m	63.6	4.0	2.0	6.1	2.0	0.5	5.2	3.8	1.5	0.0	Tr	2.5	2.5	0.0	16.5	Fluvial Sheetflood
5/ 2 m	61.5	4.4	2.3	4.7	1.8	0.4	11.9	2.6	9.4	0.0	0.0	5.6	5.6	0.0	9.1	Flood Plain / Playa
6/ 2.5 m	62.4	7.7	2.4	2.2	2.4	0.4	8.9	1.3	7.6	0.0	0.0	7.4	7.4	Tr	7.4	Flood Plain / Playa
7/ 3 m	58.2	1.2	3.7	2.7	1.2	1.4	6.3	1.2	5.1	0.0	0.0	2.3	2.3	0.0	16.3	Fluvial Ribbon Channel
8/ 3.5 m	61.4	7.0	10.3	2.4	0.3	0.7	0.8	0.3	0.5	0.0	0.0	2.5	2.5	0.0	16.1	Fluvial Ribbon Channel
9/ 4 m	57.2	5.2	4.6	2.4	1.2	0.0	12.7	9.4	3.3	0.0	Tr	6.5	6.5	0.0	11.6	Flood Plain
10/ 4.5 m	58.7	6.4	6.9	5.1	0.8	0.5	2.6	0.8	1.9	0.0	0.0	5.1	4.6	0.5	15.0	Flood Plain
11/ 5 m	53.8	4.2	2.9	4.0	0.5	1.3	16.3	10.6	5.7	0.0	Tr	11.8	11.4	0.4	5.3	Flood Plain
12/ 5.5 m	57.2	2.7	5.7	4.7	0.7	2.0	10.5	4.7	5.8	0.0	0.0	8.4	8.4	0.0	10.9	Fluvial Ribbon Channel
13/ 6 m	60.1	3.5	7.5	3.5	1.7	0.9	4.5	0.0	4.5	0.0	0.0	3.6	3.6	0.0	16.1	Fluvial Ribbon Channel
14/ 6.5 m	56.3	3.1	8.3	3.6	1.4	0.5	11.3	5.0	6.3	0.0	0.0	2.7	2.7	0.0	14.2	Fluvial Ribbon Channel
15/ 7 m	62.3	4.8	4.7	3.1	0.3	0.4	11.4	3.1	8.3	0.0	0.0	6.9	6.5	0.4	6.4	Flood Plain
16/ 7.5 m	62.4	2.7	2.5	1.7	2.5	1.0	15.2	6.3	8.9	0.0	0.0	9.5	9.1	0.4	3.9	Flood Plain
17/ 8 m	59.1	3.2	8.5	1.2	3.7	2.0	7.1	0.0	7.1	0.0	Tr	3.8	3.8	0.0	14.0	Fluvial Ribbon Channel
18/ 8.5 m	60.6	5.8	6.3	2.5	2.0	1.5	6.3	0.5	5.8	0.0	0.0	2.7	2.7	0.0	13.6	Fluvial Ribbon Channel
19/ 9 m	63.9	7.8	3.1	3.4	0.8	1.1	4.6	0.0	4.6	0.0	Tr	2.3	2.3	0.0	14.0	Fluvial Ribbon Channel
20/ 9.5 m	61.8	3.0	5.2	4.2	1.5	1.3	5.4	2.7	2.7	0.0	0.0	7.1	7.1	0.0	11.8	Fluvial Sheetflood
21/ 10 m	60.9	4.3	9.1	1.8	0.0	1.1	5.7	0.3	5.4	0.0	0.0	3.2	2.7	0.5	15.4	Fluvial Sheetflood
22/ 10.5 m	55.9	3.3	7.2	1.2	3.1	0.4	13.4	3.5	9.9	0.0	0.0	7.3	7.3	0.0	10.0	Fluvial Sheetflood
23/ 11 m	60.7	3.4	8.3	0.7	0.7	0.5	9.6	3.7	5.9	0.0	0.0	2.3	2.3	0.0	15.1	Fluvial Sheetflood
24/ 11.5 m	52.5	6.8	4.8	0.7	3.1	0.4	13.5	4.8	8.7	0.0	0.0	9.6	9.2	0.4	8.8	Fluvial Sheetflood
25/ 12 m	58.3	5.1	3.5	0.9	3.5	1.1	14.5	6.8	7.7	0.0	0.0	2.2	2.2	0.0	11.7	Fluvial Ribbon Channel
26/ 12.5 m	51.2	6.8	8.8	0.9	2.5	2.0	12.9	9.2	3.7	0.0	Tr	1.8	1.8	0.0	14.2	Fluvial Ribbon Channel
27/ 13 m	55.9	4.8	6.1	0.2	1.4	1.3	16.6	5.9	10.6	0.0	0.0	6.6	6.2	0.4	8.0	Fluvial Sheetflood
28/ 13.5 m	61.5	6.8	1.7	0.5	1.7	0.8	14.5	3.0	11.5	0.0	0.0	9.0	8.2	0.8	3.1	Fluvial Sheetflood
29/ 14 m	67.5	5.0	1.2	0.7	3.5	0.4	9.4	0.7	8.7	0.0	0.0	3.9	3.9	0.0	9.5	Fluvial Sheetflood
30/ 14.5 m	56.9	4.9	8.0	0.7	2.8	1.4	8.0	2.1	5.9	0.0	Tr	2.7	2.7	0.0	16.2	Fluvial Ribbon Channel

(continued)

Table 1. *(Continued)*

Sample location/ height	Detrital mineralogy						(Authigenic) blocky cement			Authigenic clay					Porosity	Facies association*
Lower Annan	Total qtz	Total fspr	Meta lith	Ig lith	Total mica	Smectite/mixed clay	Total blocky cem	Calcite	Quartz	Fe dolomite	Haematite	Total clay cem	Illite/mixed layer I/S	Kaolinite		
31/ 15 m	63.6	2.9	1.9	2.2	5.3	1.4	5.2	1.9	3.3	0.0	0.0	2.2	2.2	0.0	15.4	Fluvial Ribbon Channel
Upper Annan																
1/ 0 m	68.0	3.3	3.6	1.3	2.5	0.9	4.6	0.0	4.6	0.0	Tr	2.3	2.3	0.0	14.6	Fluvial Ribbon Channel
2/ 0.5 m	68.0	3.3	2.0	0.8	0.8	1.1	8.0	0.0	8.0	0.0	0.0	4.1	4.1	0.0	13.8	Fluvial Ribbon Channel
3/ 1 m	64.3	6.2	3.5	0.5	1.2	0.9	6.4	1.0	5.4	0.0	0.0	3.6	3.2	0.5	14.8	Fluvial Ribbon Channel
4/ 1.5 m	61.2	4.3	6.0	0.2	2.2	2.2	5.0	0.5	4.5	0.0	Tr	2.7	2.7	0.0	17.9	Fluvial Ribbon Channel
5/ 2 m	62.4	4.9	4.4	1.5	2.2	1.1	6.7	0.5	6.2	0.0	0.0	3.6	3.6	0.0	14.9	Fluvial Ribbon Channel
6/ 2.5 m	61.3	4.4	4.9	0.5	0.7	1.9	7.5	0.0	7.5	0.0	Tr	2.5	2.5	0.0	16.9	Fluvial Ribbon Channel
Kirklinton																
1/ 0 m	60.6	2.2	3.2	1.5	0.9	2.8	4.9	1.2	1.8	1.8	Tr	4.4	3.9	0.5	20.7	Damp Interdune
2/ 0.5 m	61.0	2.5	3.6	0.9	0.0	3.9	1.9	0.0	1.9	0.0	Tr	1.6	1.6	0.0	26.6	Aeolian Dune
3/ 1 m	58.1	3.1	2.4	2.9	1.3	4.6	2.0	0.0	1.6	0.5	Tr	1.8	1.8	0.0	25.9	Aeolian Dune
4/ 1.5 m	62.3	2.7	3.7	4.6	2.9	5.9	4.2	0.0	1.1	3.1	0.0	1.5	1.5	0.0	13.7	Aeolian Dune
5/ 2 m	64.2	4.0	3.0	3.7	1.2	2.7	6.2	0.5	3.9	1.8	Tr	1.4	1.4	0.0	15.0	Aeolian Dune
6/ 2.5 m	71.7	2.4	1.6	2.9	1.0	2.1	8.8	0.0	5.3	3.5	0.0	1.1	1.1	0.0	9.5	Aeolian Dune
7/ 3 m	57.5	4.9	4.2	3.5	2.6	4.6	3.6	0.2	2.9	0.5	Tr	0.0	0.0	0.0	20.8	Aeolian Dune
8/ 3.5 m	66.1	2.5	2.8	4.6	3.0	3.2	5.0	0.0	3.2	1.8	0.0	4.0	4.0	0.0	10.1	Aeolian Dune
9/ 4 m	62.4	3.0	1.8	1.4	1.4	4.5	3.4	0.2	2.7	0.4	0.0	3.1	2.7	0.4	21.4	Aeolian Dune

The identification of authigenic minerals, such as authigenic illite, was aided using a mixture of SEM and SEM-CL. Total quartz is >95% monocrystalline quartz with trace polycristalline quartz, total feldspar is >95% K-feldspar with trace plagioclase, Meta lith (metamorphic lithic), Ig lith (igneous lithic), total mica is >95% muscovite with trace biotite.

geological processes, so care is taken in the order in which analyses are made for each rock chip. If resetting has occurred, larger inclusions may give higher temperatures, homogenization temperature distributions may show a high temperature tail and data from paragenetically distinct settings may overlap. Final melting occurs at the disappearance of the last trace of solid in the inclusion on heating (usually after cooling an inclusion to well below room temperature).

Schlumberger's burial history simulation software PetroMod (V. 2012.2) was used in this study to help reconstruct the geological evolution of the Solway and Carlisle Basins. Maximum palaeotemperatures and timing obtained from apatite fission-track analysis and palaeotemperatures obtained from fluid inclusions in mineral cements were used to help calibrate the model (Newman 1999; Floodpage *et al.* 2001).

Primary data was supplemented by the following various supporting secondary data. Firstly, offshore data within the Solway Basin was sourced from the only two hydrocarbon wells drilled within the region (wells UK 112/15-1 and IOM 112/19-1, Fig. 1). Both wells penetrated the KSF and ASF equivalents (OSF and SBSF respectively; Fig. 2), with the OSF chosen as the primary reservoir target in both wells. The data was sourced from the Oil and Gas Authority (OGA) through the National Data Repository (NDR), presented mainly through Well/Geological Completion Reports. Data from a previously produced petrographic analysis was available for well 112/19-1, which consisted of the petrography of 8 core samples and core plugs of OSF, where core plugs were cut perpendicular to apparent bedding and thin sections were prepared and point-counted for 300-counts per sample. Porosity and permeability data was taken from both wells (112/15-1 & 112/19-1), where porosity is helium porosity at 1500 psi and permeability is air horizontal permeability, each taken from a total 111 core samples. Gamma and sonic wire-line data was similarly available from both wells (112/15-1 & 112/19-1).

Secondly, data for comparison to the EISB came from six wells in the North and South Morecambe fields (wells 110/2a-N1, 110/2a-8, 110/2a-7, 110/2-6, 110/2a-F1 and 110/3a-A3). All wells were drilled through the OSF and to the top SBSF (KSF and top ASF, respectively; Fig. 2). Petrographic analysis data was available for 443 samples across the numerous wells. The petrographic methodology was similar, utilizing core plugs and core samples. Porosity measurements were conducted using a Ruska parameter. Permeability is horizontal permeability calculated using dry nitrogen. Grain size data for the EISB came from well 110/2-6.

Finally, a further four thin section samples of SBSF from Fleswick Bay in West Cumbria (NX 945132) sourced from Durham University are used for an onshore EISB comparison.

Results

Onshore analogue petrography

The depositional facies for the ASF and KSF of the SSG of the Solway Basin have been described by several previous authors (e.g. Akhurst *et al.* 1997; Newman 1999; Holliday *et al.* 2001, 2004; Brookfield 2004, 2008). The sandstones of the ASF are very fine-grained, sub-angular to sub-rounded, moderately mature and moderately to well sorted sublithic arenites with minor feldspathic subarkoses (Folk Classification; Figs 5a and 6). The detrital mineral assemblage is dominated by quartz, lithic clasts, K-feldspar, and illite and smectite matrix clays, with minor muscovite and biotite. Compositionally, the Lower and Upper ASF sampled from Cove Quarry and Glinger Burn, respectively, show a distinct compositional difference. The Upper ASF features a higher level of compositional maturity, where the average quartz abundance normalized to the total quartz, feldspar and lithic content of the Lower and Upper ASF is 82.0% and 87.5%, respectively (Figs 4 and 6).

Comparison of the ASF to the stratigraphically equivalent onshore outcrops of the RSM at Fleswick Bay, Cumbria, shows that the latter are coarser and cleaner (contain less clay), where the stacked channel sandstones contain only trace (<1%) matrix and pore filling clays (Fig. 7).

The sandstones of the KSF are fine-to medium-grained, sub-angular to well rounded, mature, well sorted, sublithic arenites to marginal quartz arenites (Folk Classification; Figs 5b and 6). The detrital mineral assemblage is remarkably similar to that of the ASF, and the only discernible difference is a general reduction in lithic clasts, feldspar and mica and an increase in detrital smectite (discerned from SEM). For both the ASF and KSF total feldspar is >95% K-feldspar with only trace plagioclase. Compositionally, the onshore KSF shows a significantly higher maturity (average relative quartz abundance of 88.3%) compared to the Lower ASF and a marginally higher maturity compared to the Upper ASF (Fig. 6). Compositional maturity between the onshore and offshore KSF/OSF (Cliff Bridge and well 112/19-1) within the Solway Basin

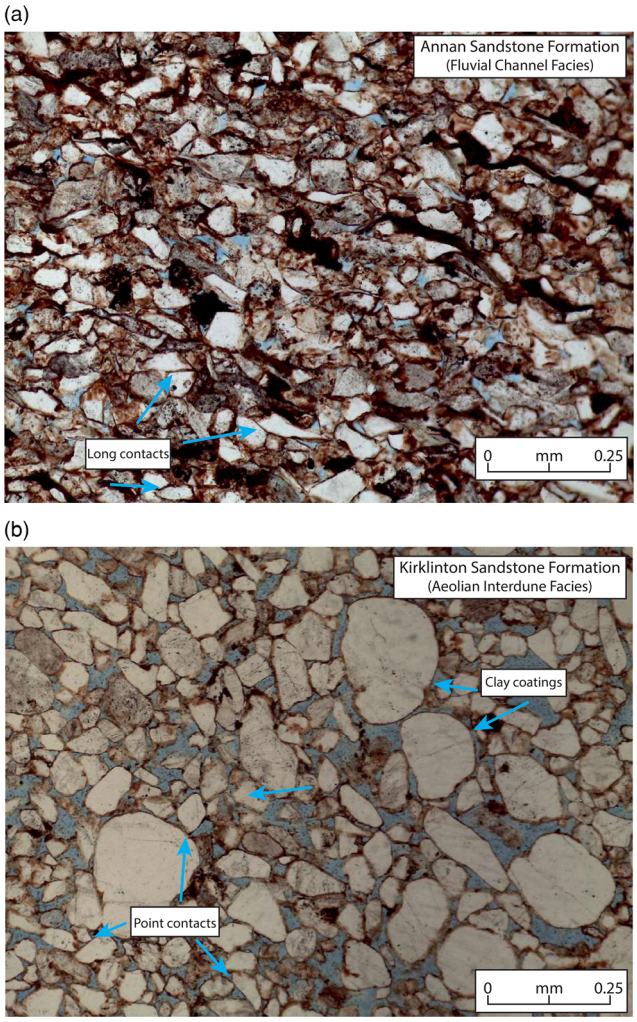

Fig. 5. Photomicrographs of (**a**) a fluvial channel deposit within the ASF from Cove Quarry and, (**b**) an aeolian interdune deposit within the KSF at Cliff Bridge. The sandstones of the ASF are poorly sorted and demonstrate a high degree of compaction. The KSF is better sorted and features a bi-modal distribution of quartz grains between fine and medium grade sand, the latter being well rounded and frosted. The blue-dye indicates void space and demonstrates a higher porosity to the ASF. Characteristic 'long' and 'point' contacts, as well as clay grain coatings, which are suggested to have preserved porosity, are identified.

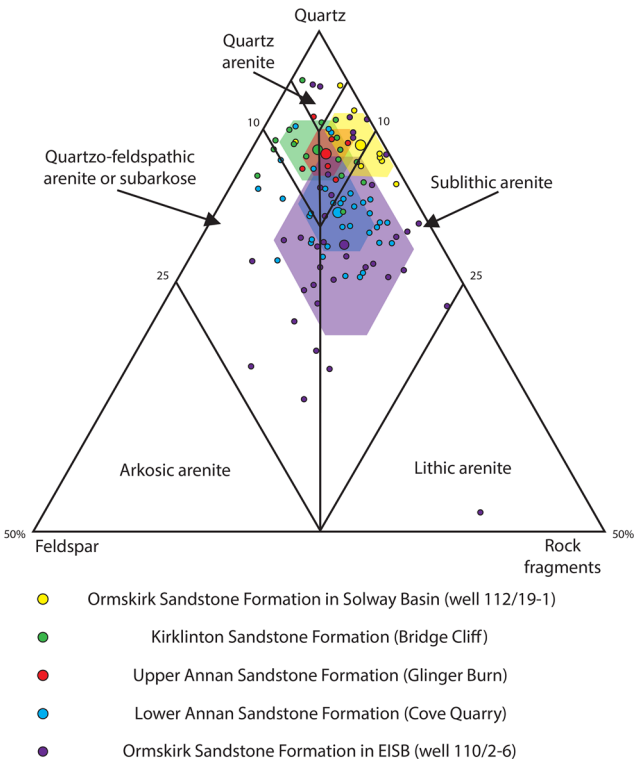

Fig. 6. Ternary diagram showing the detrital mineralogy of the Lower and Upper ASF and the KSF in the SSG sourced from the onshore outcrops seen in Figure 1. Also shown is the detrital mineralogy of the OSF (KSF Equivalent) found in EISB well 110/2-6 and Solway well 112/19-1. Larger dots represent mean values and shaded regions represent the standard deviation range for that sample.

corresponds well, where the offshore KSF/OSF (well 112/19-1) has an average relative quartz abundance of 88.8%. The analogous OSF in the EISB shows a noticeable reduction in maturity in comparison with an average relative quartz abundance of 78.5% (Well 110/2-6) (Fig. 6). Similarly, the KSF shows a prominently higher roundness and sphericity of its grains, especially those of medium sand grade.

The ASF and KSF are composed of fluvial and aeolian faces, respectively, forming lithostratigraphic boundaries (e.g. Holliday *et al.* 2004). The fluvial facies associations discerned here are dominantly fluvial sheetflood sandstones, characterized mainly by vertical lamination and ribbon channel sandstones, characterized by trough cross-bedded erosional based units. Both units form multistorey channel sandstone units with sheet and ribbon geometries. The fluvial ASF is also associated with flood plain facies associations, characterized by silt and mudstone deposits with rootlet traces. Playa facies are further discerned from flood plain facies because of their prominence in distal fluvial successions and in aeolian environments, where they are identified by desiccation structures and symmetrical ripples (Figs 3a and 4; Table 1). KSF aeolian facies associations identified are characteristic dune structures as described previously and damp interdune facies with wavy bedding and playa facies (Fig. 3b; Table 1).

Offshore Solway petrography

The SBSF within the offshore Solway Basin has a maximum proven thicknesses of *c.* 1072 m within well 112/15-1, where core sampling reports divide the SBSF into the 'Lower St Bees' and 'Upper St Bees'. The 'Lower St Bees' is predominantly a red brown very fine to fine, locally medium grained sandstone that is very clay rich, with silt and chert beds at its base and anhydrite intermittently present throughout. The 'Upper St Bees' is a much cleaner very fine to fine, occasionally fine to medium grained sandstone that is very friable and ferruginous in parts. The OSF is proven to be *c.* 175 m thick in well 112/15-1. It is composed of red to orange-brown fine to medium, locally coarse-grained sandstones with frosted grains, that are very friable and ferruginous and contain halite and anhydrite evaporite beds at its top.

Lithological differences between the 'Lower' and 'Upper' St Bees are similar to those identified by Jackson *et al.* (1987) in the EISB and likely represent a change from the RSM to CSM of the SBSF, which is identifiable in the EISB and Sellafield area through geophysical data (gamma and sonic velocity values) (Fig. 2). The assumed 'Top Silicified Zone' was found within well 112/19-1 to prove thicknesses of 297 m and 420 m, respectively for the RSM and CSM.

Porosity and permeability

Porosities range from near 2% to 25% and from 14% to 28% for the ASF and KSF, respectively (Fig. 8a). These ranges are comparable to the equivalent facies in the EISB (Fig. 9; Meadows and Beach 1993*a*; Quirk *et al.* 1999). The permeability ranges for the sandstones are 0.5–300 mD for 'wet' facies (mainly ASF), including wet sandflat, wet sheetflood, and fluvial channels, whilst 'dry' facies range from 100–5000 mD and encompass dry sandflat and dry aeolian facies (mainly KSF) (see Newman 1999).

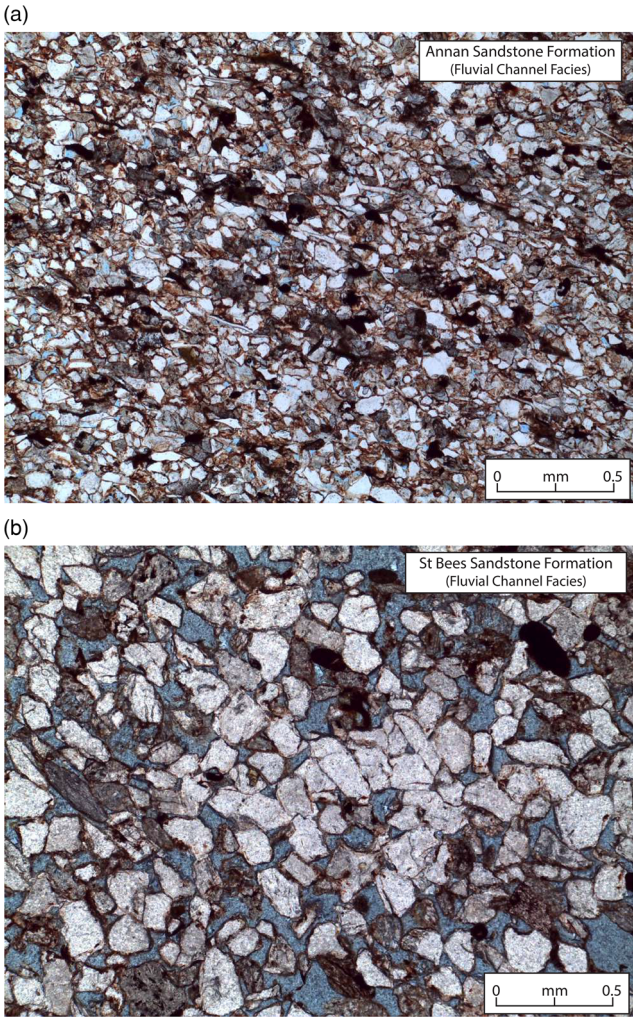

Fig. 7. Photomicrographs of (**a**) a channel sandstone deposit within the ASF from Cove Quarry and, (**b**) a channel sandstone deposit within the equivalent SBSF at Fleswick Bay, West Cumbria. The channel sands at Cove Quarry are muddier and feature increased compaction, with a visible fabric.

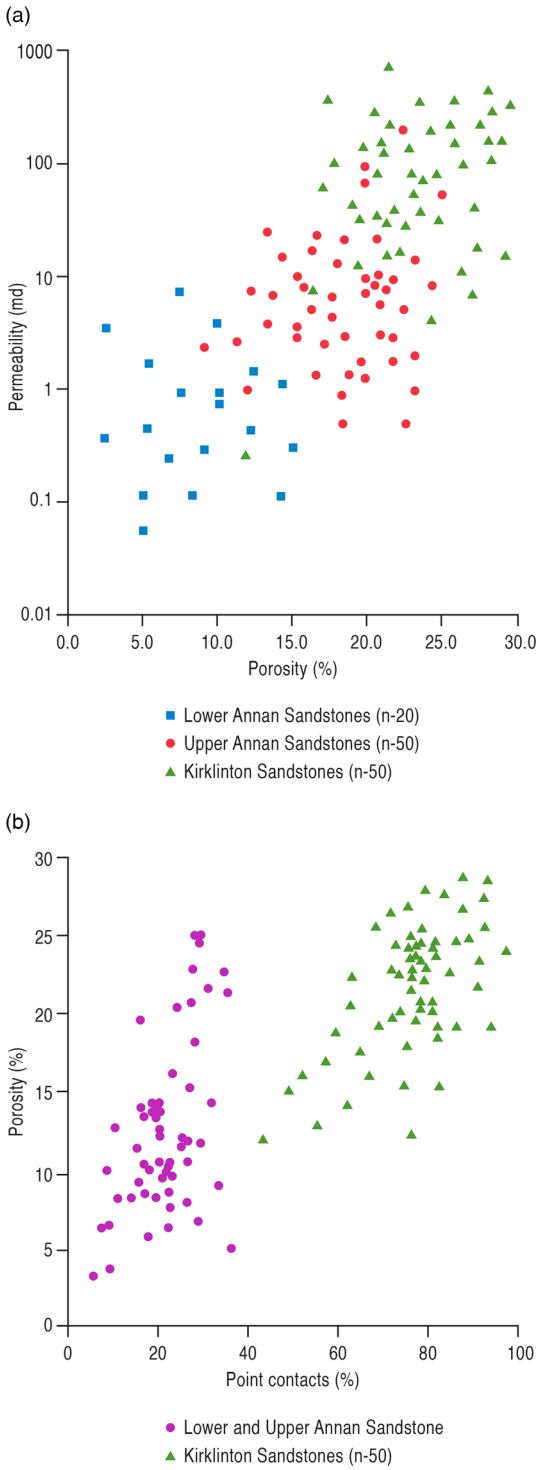

Fig. 8. (**a**) Porosity and permeability cross-plot for the ASF and KSF, SSG. A portable hand-held mechanical mini permeameter was used for rapid in-situ determination of permeability at outcrop and on fresh hand specimens with >120 measurements taken (Chandler *et al.* 1989), (**b**) cross plot of porosity and percentage of detrital grain point contacts. Note the strong effect of compaction on the ASF, resulting in a greater degree of long contacts with a direct correlation between grain contacts and porosity.

The extent of compaction observed in the primary outcrop-collected petrographic samples from the ASF and KSF varies markedly. The ASF has experienced significantly more compaction, with an average of 85% long contacts in the fluvial facies (Figs 5a and 7a). This contrasts with the sandstones within the KSF that have undergone considerably less compaction and have an average of 24% long contacts (Fig. 5b). Petrographic and SEM analysis has revealed no significant dissolution of grains in either formation. Point contact preservation shows a direct correlation with higher porosity preservation between the ASF and KSF (Fig. 8b).

It is recognized that the porosities of the ASF are noticeably lower than those of the KSF, this being a combination of porosity loss due to compaction and cementation effects (Fig. 10). The use of a division line between compactional and cementational porosity loss illustrates that porosity loss for most of Upper ASF is cementational, whilst porosity loss for most of the KSF is compactional (Fig. 10).

Analysis of data from the two Solway wells shows the OSF has an average porosity and permeability of 15% and 503 mD, respectively. However, significant variation was found within the values. Using core samples and geophysical wire-line values it was determined that 'dry' (mainly aeolian) facies had an average porosity and permeability of 18% and 1024 mD (range up to 7782 mD), respectively, and 'wet' (mainly fluvial channel but also playa and flood plain) facies had an average of 13% and 125 mD (range up to 833 mD), respectively. Specifically, it is reported that aeolian dune facies exhibit the best reservoir quality with a mean porosity and permeability of 19.8% and 1176 mD. Within the dry facies, permeability was compromised significantly in beds containing evaporites (dominantly anhydrite and minor halite), which additionally compromised the net:gross (N:G) of the top 26 m in well 112/19-1, giving it an overall value of 65% (Newman 1999). Despite also containing evaporites at the top of the Formation, the OSF in well 112/15-1 has a N:G of 81%. The limited data available for the SBSF shows a range of porosity and permeability values of 8% to 17% and >0.1 to 26 mD, respectively, with lower values interpreted to be related to mudstones and fine-grained floodplain facies. Permeability values are particularly low within wet facies and below the Top Silicified Zone, in the clay rich RSM. Within the upper ASF of well 112/19-1 however, which features stacked channels and a more 'dry' facies geophysical signature, the N:G is reported as 77%.

Grain size and sorting

Two distinct grain size populations are discerned. Both the Lower and Upper ASF are composed of very fine sand grains, which constitute *c.* 70% of detrital grains, with a minor proportional increase in fine sand grains within the Upper ASF (Fig. 11a). The second population displays a grain size bimodality within the KSF, with fine-sand sized detrital grains constituting 60–65% and the remainder medium-grained in size, forming a mean grain size that falls roughly between the two (Fig. 11a). Pore diameter values over the range 0.03–0.15 mm were measured and are micropores according to the classification scheme proposed by Katsube *et al.* (1999*a*, *b*) (Fig. 11b). The texturally mature, yet mineralogically sub-mature sandstones of the ASF and KSF are petrographically comparable to the contemporaneous SBSF and OSF of the EISB (Fig. 6; Meadows and Beach 1993*b*; Meadows 2006).

Much like the Ormskirk Sandstone in the EISB (Meadows and Beach 1993*a*), there is a tendency for grains of larger sizes to occur more commonly in the aeolian facies of the KSF, which can be found in the foresets of dunes and deflation surfaces. However, this is counter-balanced by the presence of very fine sand laminae in the same sequences. The sorting of the sandstones varies substantially from moderate to good for both the fluvial and aeolian facies, respectively, however the aeolian sandstones are well or locally very well sorted.

The difference in grain types encountered, in terms of angularity and sphericity, is significant between the ASF and KSF. The aeolian grains of the KSF are very well rounded and exhibit a high degree of sphericity, forming a major component of the facies (Fig. 5b). In comparison, the ASF grains are sub-angular to sub-rounded and exhibit a low degree of sphericity that is common for much of the fluvial facies (Fig. 5a).

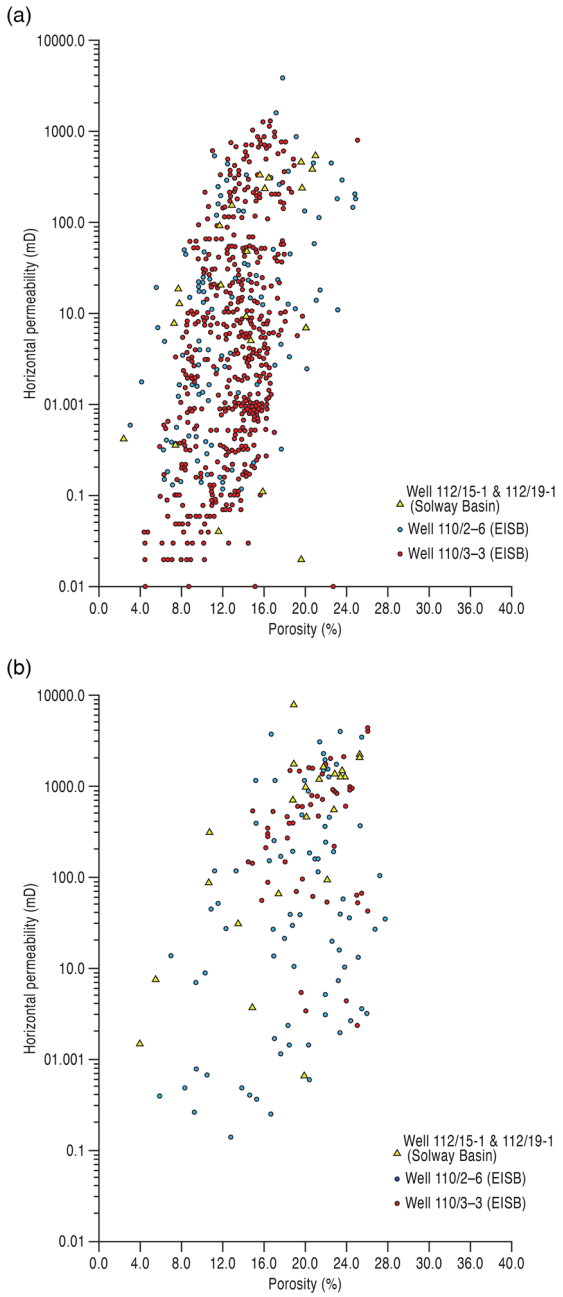

Fig. 9. Porosity and permeability cross-plots from conventional core analysis data for well 110/2-6 and 110/3-3, EISB and 112/15-1 and 112/19-1, Solway Basin. The plots relate to the major sandstone facies (**a**) fluvial and, (**b**) aeolian of the OSF (after Meadows and Beach 1993*a*).

The higher porosities in the ASF are encountered within the ribbon channel facies which preserve moderate reservoir quality. The lowest porosities and permeabilities within the ASF are accounted for by the very fine-grained nature of flood plain samples, which possess poor reservoir quality (Fig. 8; Table 1).

Similarly, within the offshore Solway Basin, high porosity and permeability values are found within the spherical, well-rounded grains of the aeolian dune facies, whilst lower values are found within wetter facies which are finer grained, with reduced pore size and higher clay content.

Diagenesis and reservoir quality

All previous studies of the detailed diagenesis for the SSG have been focused on the EISB (Burley 1984; Macchi *et al.* 1990; Meadows and Beach 1993*a*; Meadows 2006; Medici *et al.* 2019) or the Corrib and Slyne Basins to the West of Ireland (Schmid *et al.* 2004; Dancer *et al.* 2005). These two Basins were documented separately as detailed provenance studies using Pb isotopes of K-feldspars has shown they were separate, although the EISB and Solway were likely linked (Tyrrell *et al.* 2012). New observations and interpretations relevant to the impact of diagenesis on reservoir quality and porosity preservation, from the SSG of the Solway and Carlisle Basins, are described here.

The mineralogy of the ASF and KSF of the Solway Basin have undergone significant diagenetic alteration. Authigenic minerals occupy an average of *c.* 15% of the rock volume. The main diagenetic processes that have affected the sandstones include mechanical and chemical compaction, the precipitation of quartz, calcite, mixed layer smectite–illite clays, minor dolomite and kaolinite, as well as dissolution of unstable grains such as feldspar.

Kaolinite occurs as pseudohexagonal, vermicular booklets and is found in both the ASF and KSF, contributing to <1%. SEM evidence suggests kaolinite precipitation is linked to feldspar dissolution, where kaolinite is found precipitated within or around partially dissolved feldspar grains (Fig. 12a). Where kaolinite is present, it does exhibit a slight detrimental effect on porosity and tends to occur more widely in the fluvial ASF, mainly in the flood plain and sheetflood facies (Table 1).

Very little chlorite (<1%) is found in any of the studied sections unlike in other SSG sequences (e.g. Schmid *et al.* 2004; Dancer *et al.* 2005).

The red colour of the sandstones in this study reflects the presence of fine-grained haematite precipitated on the surface of the detrital grains. No noticeable differences in colour were documented between facies in either the ASF or KSF.

The major cement phases in the ASF and KSF are clay (mainly illite and mixed layer illite–smectite), calcite (non-ferroan and ferroan composition) and quartz, which are discussed in more detail below (Table 1).

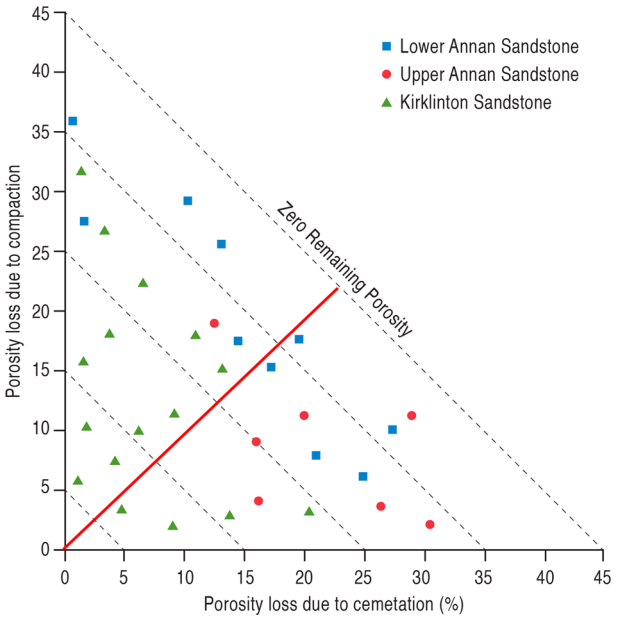

Fig. 10. Effect of compaction and cementation on porosity loss of the ASF and KSF sandstones. Diagram and calculation after Houseknecht (1987), using the methodologies 'Calculation of Compactional Porosity Loss (COPL)' and 'Cementational Porosity Loss (CEPL)' based on petrographic data (including porosity). A division line forms a boundary between compactional and cementational porosity loss, illustrating that porosity loss for most of Upper ASF is cementational, whilst porosity loss for most of the KSF is compactional.

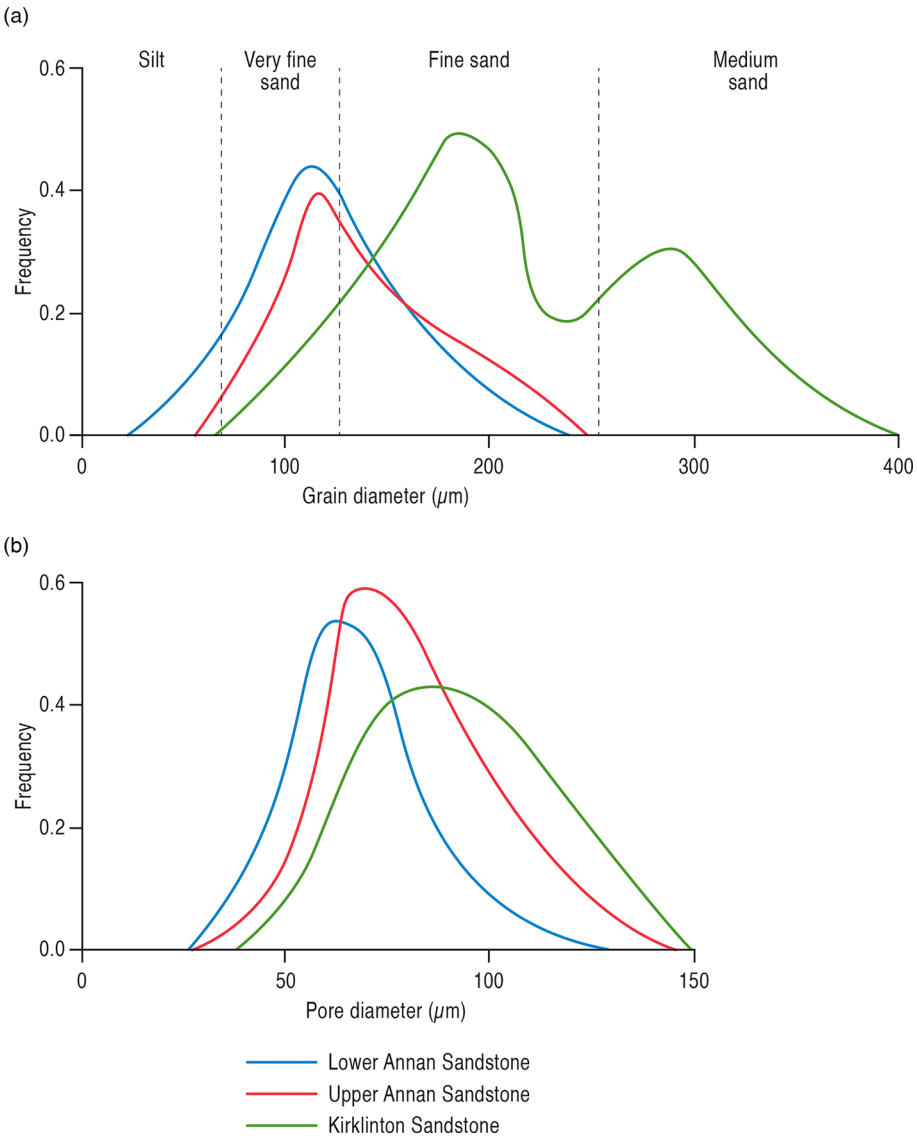

Fig. 11. Distribution of (**a**) grain size and (**b**) pore size of ASF and KSF sandstones.

Quartz cements

Quartz cements in the Solway Basin sandstones take the form of euhedral to prismatic, syntaxial macroquartz overgrowths, typically between 5–20 μm but can reach 80 μm in size (Fig. 12b). Thin section analysis clearly reveals that quartz cements precipitate directly upon, and therefore post-date, early haematite coatings which were observed coating detrital framework grains, in the ASF and KSF (Fig. 5a, b). There is a clear facies control upon the distribution of quartz overgrowths. Whilst these cements are found within the aeolian KSF (*c.* 4%), they are more common throughout the fluvial ASF (*c.* 8–12%), a finding that accords with a similar facies control on quartz diagenesis in the EISB (Meadows and Beach 1993*a*; Greenwood and Habesch 1997).

Calcite cements

Two stages of calcite cement are recognized within the ASF. These cements are:

(1) Early non-ferroan calcite cement forming aggregates of interlocking crystals directly coating detrital grains surfaces that are not found as isolated crystals within pore space. Crystals form blocky to euhedral micro-crystals and are typically *c.* 10–20 μm in length (Fig. 12c).

(2) Later stage non-ferroan and ferroan calcite cements are distributed as isolated, blocky to granular, sparite crystals and form both within pore spaces of detrital grains and on detrital grain surfaces. These cements are noticeably larger than earlier formed calcite cements and are typically *c.* 30 μm in length, forming well developed, euhedral crystals (Figs 12c and 13a).

Calcite cement forms a significant proportion (up to 13%) within the ASF and appears to be facies controlled. Greater percentages of this calcite cement are found in flood plain and subordinately sheetflood facies of the ASF and are only locally identified in the aeolian KSF, within damper aeolian facies (Table 1). Where found, these cements severely occlude pore space. The sandstones of the KSF only show minor evidence for late-stage calcite cementation, forming similar euhedral cements as described above within the ASF (Fig. 13a; Table 1). Calcite rarity within the KSF similarly correlates with the offshore KSF sample mineralogy from well 112/19-1, where calcite is found in abundances of <0.5%.

Ferroan dolomite only occurs in the KSF as *c.* 5–30 μm wide euhedral rhombs. Ferroan dolomite being the sole or dominant carbonate species is similarly seen within the offshore KSF (well 112/19-1) and within the equivalent OSF within the EISB Morecombe Bay. The ferroan dolomite is always pore-filling and can be associated with illite cements and fibres (Fig. 13b–d). BSEM, optical microscopy and CL-SEM analyses reveal that the

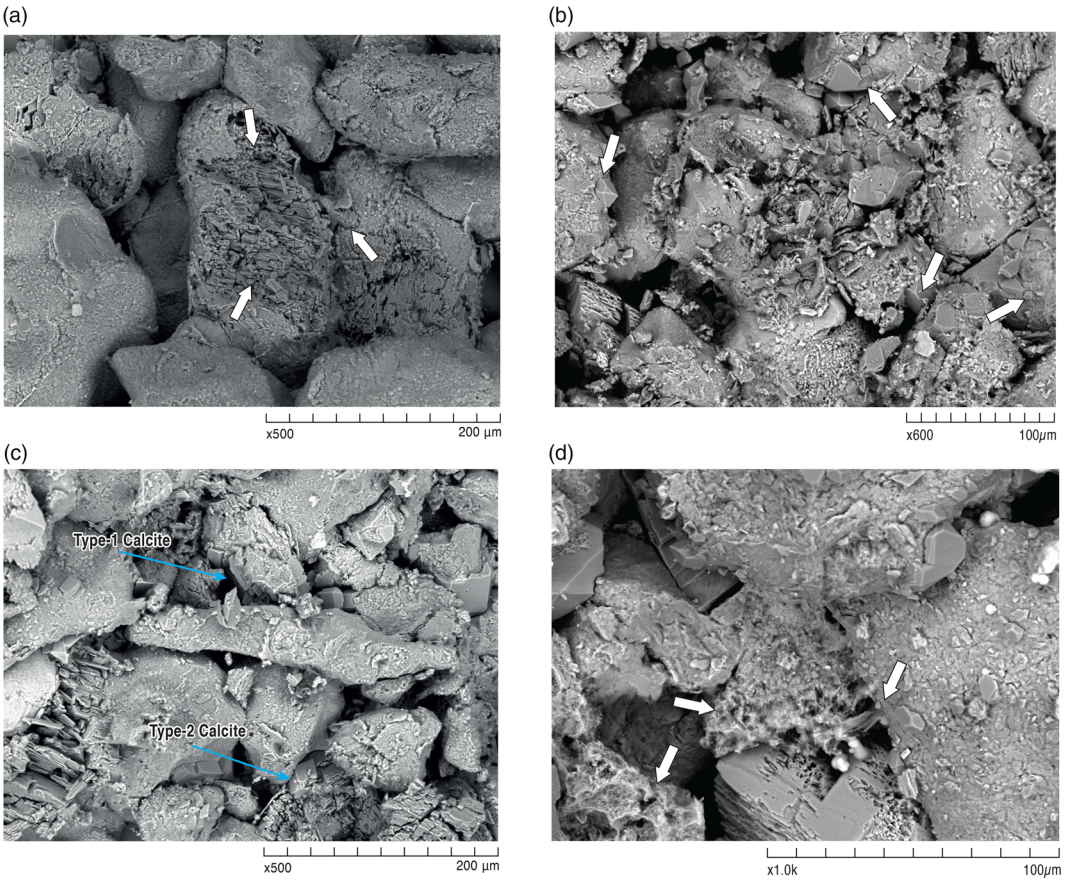

Fig. 12. SEM image of ASF showing; (**a**) partial K-feldspar dissolution with associated pseudohexagonal, vermicular kaolinite booklets within pore space, (**b**) macroquartz overgrowths, (**c**) two types of calcite cement; calcite-I is an early non-ferroan calcite cement which forms aggregates of interlocking crystals, typically *c.* 10–20 µm in length; calcite-II is a later stage non-ferroan calcite, formed of isolated, blocky to granular, sparite crystals, typically *c.* 30 µm in length, **(d)** occurrence of illite–smectite clays is common which both coat detrital grains and, especially illite, frequently occulde pore throats.

dolomite occurs around detrital carbonate nuclei. The morphology shows little variation through the KSF and always occupies <2% of the rock by volume (Table 1). Interestingly, dolomite only forms a very minor component of the KSF but forms a major component in other SSG sequences, such as in the Corrib Field where it is the most abundant cement (up to 25% of the rock volume, with a mean of 10%) and has been found to be paramount in controlling reservoir quality (Schmid *et al.* 2004). Local abundances of ferroan dolomite were found in the offshore Solway Basin KSF however, with the greatest abundances located in the damp and wet sandflat facies.

Smectite and illite

Detrital smectite is abundant within the KSF, whilst minor amounts are found in the ASF, and was distinguished from mixed unresolved clays by SEM (Table 1). This is unsurprising, since previous studies demonstrate that smectite is the as this is the dominant weathering product in recent and Triassic desert environments (e.g. Weibel and Grobety 1999; Lybrand and Rasmussen 2018; Al-Juboury *et al.* 2020) and was likely a detrital and infiltrated clay. Authigenic smectite is found as mostly mixed-layer smectite–illite where it often forms clay coatings (Fig. 5b). This mixed layer smectite–illite additionally forms a honey-comb texture with protruding illite fibres and can be pore-occluding and pore-filling (Fig. 12d).

Illite is abundant in the fluvial ASF (*c.* 5%), with greater abundances found in the fine grained sheetflood and flood basin facies. Authigenic illite is observed on all clay-coated and uncoated detrital grains and on clay cutans and bridges, although rarely present on euhedral faces of quartz overgrowths (Fig. 12d). Authigenic illite tends to nucleate from a single thin veneer precipitated upon detrital grains and tend to grow as independent strands and fibres that extend into the pore space of host sandstones. Illite also commonly adapts a pore bridging habit, linking and connecting detrital framework grains. Where this is the case, pore space is not as severely occluded. Illite fibres generally have a length of *c.* 20 µm. This is the case both when illite occurs as isolated fibres and when illite is documented as mixed layer smectite–illite cement (Fig. 12d).

Stable isotope results for calcite and dolomite cements

Figure 14 illustrates the range of $\delta^{13}C$ and $\delta^{18}O$ for the calcite cement in the ASF and the ferroan dolomite cement in the KSF.

The early and later stage calcite cement have been analysed for the ASF and the distribution of data may reflect the two different generations of calcite cement. No systematic relationship to location or facies (e.g. ribbon v. sheet sandstones) is evident in the data. The calcite cement ranges from $\delta^{18}O_{PDB}$ −10‰ to − 3.5‰ and $\delta^{13}C_{PDB}$ − 5.8‰ to +0.3‰ (Fig. 15a). Ferroan dolomite only occurs in the KSF and shows no variation within the sandstone sections. The ferroan dolomite cement analysed ranges from $\delta^{18}O_{PDB}$ −10.6‰ to − 3.0‰ and $\delta^{13}C_{PDB}$ − 6.9‰ to − 0.8‰ (Fig. 14b).

Also plotted for comparison are the ranges of $\delta^{13}C$ and $\delta^{18}O$ from Naylor *et al.* (1989); Morad *et al.* (1998) and Greenwood and Habesch (1997), which are sampled from the Mid-Late Triassic Lossiemouth Sandstone Formation in the Moray Firth Basin, the Late Triassic Lunde Formation in the Snorre Field of the Norwegian North Sea and the OSF from the central EISB (blocks 110/13-110/15), respectively.

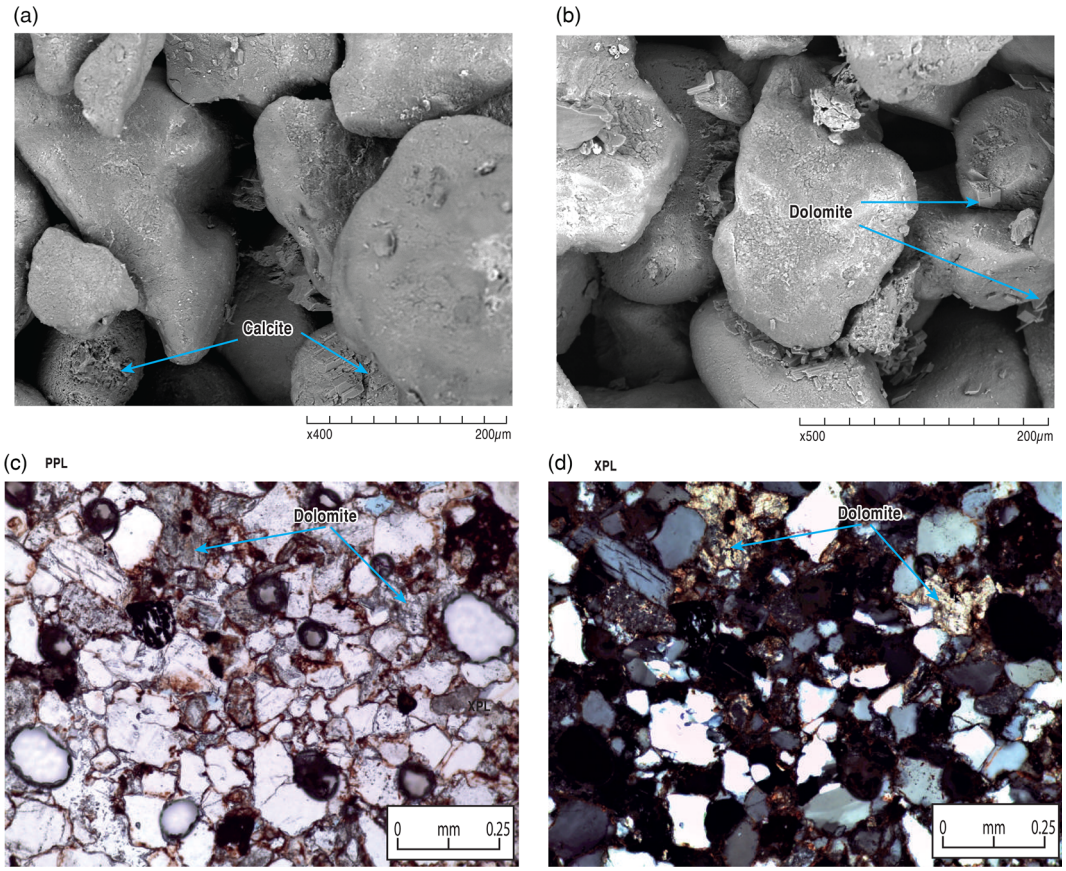

Fig. 13. SEM images from the KSF. (**a**) calcite-II cements within the KSF, which is rarer than within with the ASF and the sole calcite phase within the KSF, (**b**) ferroan dolomite that tends to be pore-filling and frequently associated with illite. Thin section photomicrograph of pore-filling ferroan dolomite in (**c**) PPL and (**d**) XPL. SEM reveals cystals typically form *c.* 5–30 μm wide euhedral rhombs.

Burial history modelling and fluid inclusion data

The geological evolution of the Solway and Carlisle Basins is presented in Figure 15. Fluid inclusion microthermometric data show that the quartz precipitated at temperatures between 95 to 125°C from formation waters with salinities of 10–18 wt% NaCl. The measurable aqueous inclusions in the dolomite cements displayed homogenization temperatures of 100 to >135°C from formation waters with higher salinities 20–25 wt% NaCl. The salinity of formation waters encountered are broadly similar to those of the EISB where the salinity is suggested to have derived from the dissolution of Permian evaporites (e.g. Greenwood and Habesch 1997).

The burial history of the Solway and Carlisle Basins does differ from that of the EISB (Floodpage *et al.* 2001). This study demonstrates that the ASF and KSF reached maximum burial depth of *c.* 2800 m during the Late Jurassic and certainly before the influence of the Cimmerian uplift (Fig. 15). However, taking an average present-day geothermal gradient of 30.2°C km^{-1} would suggest the sandstones in this study only reached a maximum burial temperature of *c.* 85°C. This temperature is significantly less than that determined from fluid inclusion analysis. If the homogenization temperatures (T_h) for the fluid inclusions are assumed to represent the minimum trapping temperature in the quartz and dolomite cements then an additional source of heat must be accounted for in the burial history.

Discussion

Timing of diagenetic processes

The relative timing of diagenetic processes is presented in Figure 16a and b, as inferred from their textural relations as observed in thin section and using the SEM. Precipitation of haematite coatings onto detrital framework grains underneath quartz overgrowths shows early precipitation. As is common with recent sediments in hot, arid to semi-arid environments, this was likely a result of early near-surface diagenesis from the alteration of iron-bearing grains and smectitic clays (Burley *et al.* 1985), where greater haematite cementation is seen and expected within the aeolian KSF.

Early dissolution of detrital K-feldspar is common within continental red beds (Walker *et al.* 1978). Similar early dissolution of feldspar within the ASF and KSF is suggested as relative to the feldspar content of the sandstones (means of 7% and 4%, respectively), secondary porosity created by feldspar dissolution is minor (1% to 2%), suggesting that many K-feldspar grains did not undergo dissolution and/or dissolution was incomplete. This interpretation is also supported by SEM analysis, whereby partial dissolution of K-feldspar is common (Fig. 12a). Secondary porosity created by K-feldspar dissolution has not led to an increase in net porosity, since the dissolved material will have on the evidence of the quantity of the cements previously described, been locally re-precipitated.

Kaolinite occurrence within the Solway Basin SSG is minor (<1%) and in other SSG rocks within NW Europe it is found to be oddly absent (Schmid *et al.* 2004). Determining the exact source of silica for its formation is therefore difficult. Based on the evidence that feldspar dissolution is linked to later kaolinite precipitation within generated pore-space, kaolinite precipitation is suggested to have occurred after early feldspar dissolution, as is a typical open system eogenetic reaction (Fig. 12a; Bjørlykke and Jahren 2012).

In the ASF, early calcite cementation is suggested by the formation of overgrowths and cements upon detrital framework

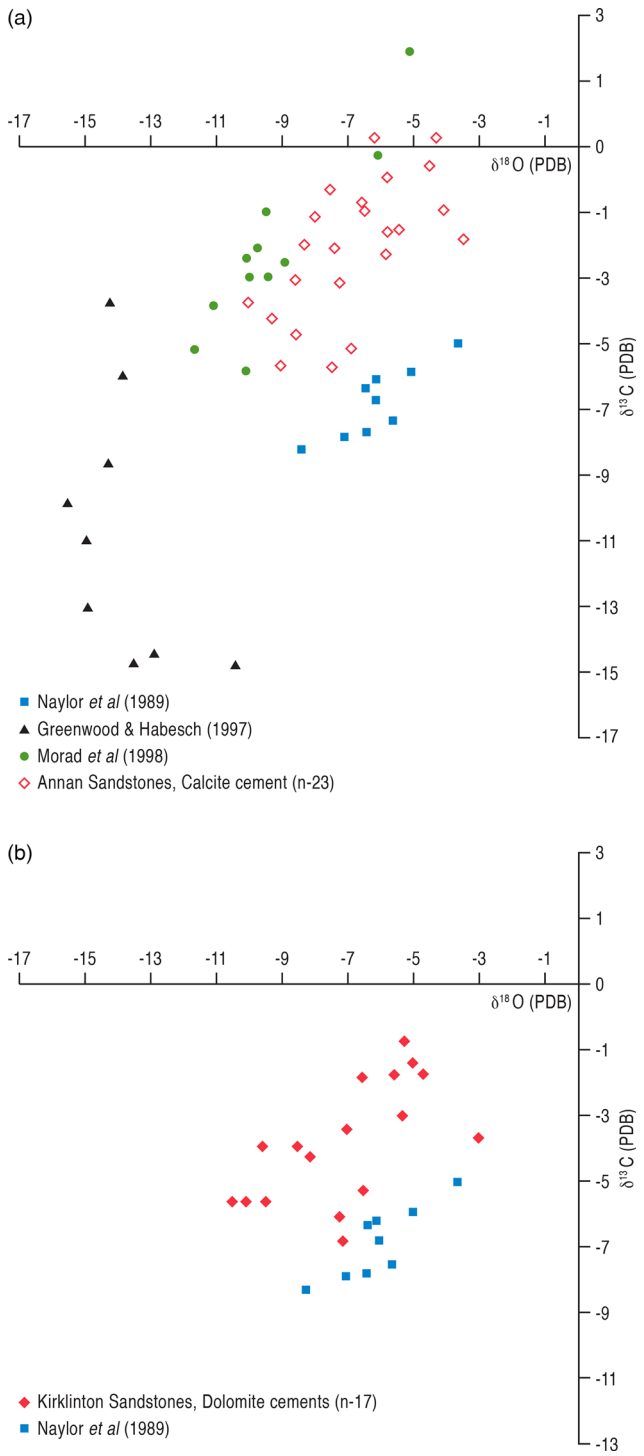

Fig. 14. Cross-plots of oxygen and carbon stable isotope data for (**a**) ASF calcite cements; and (**b**) KSF dolomite cements. Plotted for comparison are the ranges of $\delta^{13}C$ and $\delta^{18}O$ from Naylor *et al.* (1989); Morad *et al.* (1998) and Greenwood and Habesch (1997), which are sampled from the Mid–Late Triassic Lossiemouth Sandstone Formation in the Moray Firth Basin, the Late Triassic Lunde Formation in the Snorre Field of the Norwegian North Sea and the OSF from the central EISB (blocks 110/13-110/15), respectively.

grains, as has been noted in other studies of the SSG in the Irish Sea area (e.g. Strong 1993; Greenwood and Habesch 1997). The carbon and oxygen stable isotope compositions for the ASF shows two generations of this early calcite formation (i.e. calcite I and II, Fig. 14a). Data points with a more negative $\delta^{13}C$ and $\delta^{18}O$ (calcite I) composition are similar to values for Triassic calcretes from the Inner Moray Firth as reported by Naylor *et al.* (1989). This would support calcite cements preserving an isotopic signature of the early groundwater in the fluvial sediments and reflects some recrystallization of caliche, the latter of which Meadows and Beach (1993*a*) also suggested for the EISB. A later second calcite cement shows more positive $\delta^{13}C_{PDB}$ values of −5.8‰ to +0.3‰, which is more positive than those usually associated with calcretes and may indicate a carbon source dominated by atmospheric CO_2 (Cerling 1991). The more positive $\delta^{13}C_{PDB}$ compositions (from calcite II) also display a trend similar to that of the Triassic Lunde Formation of the Snorre Field, Norway (Fig. 14a, Morad *et al.* 1998). Carbon from a microbial methanogenesis oxidation of plant material and a possible contribution from atmospheric CO_2 are attributed and is a probable cause for the spread of data for the ASF.

Disparity in $\delta^{13}C$ and $\delta^{18}O$ values between the EISB from Greenwood and Habesch (1997) and the Annan Sandstones samples, and mainly the negative $\delta^{13}C$ signature of the EISB samples, are attributed to the effects of methanogenesis from a deep, dominantly thermally mature organic carbon source, related to hydrocarbon migration, seen within the EISB but which has not been identified within the Solway Basin (e.g. Newman 1999; Fig. 14a). Similarly, this was associated with a later stage calcite precipitate (calcite-III) in the EISB which is similarly not present in the Solway Basin (Greenwood and Habesch 1997).

These findings are therefore suggestive of eodiagenetic precipitation, pre-dating any significant compaction, similarly suggested by generally long and simple grain contacts (Fig. 5) with no evidence of sutured or complex contacts. During progressive burial, later stage calcite cements were precipitated over a more extended period of time, forming larger, well-developed crystals (Fig. 12c). This early cement acted as a nucleation site for later pore-filling carbonate phases, explaining the abundance of late-stage calcite cements in the ASF. Within the KSF, only a minor volume of calcite cement is found, and this is attributed to the absence of early calcite cement nucleation sites for later carbonate phases (Meadows and Beach 1993*a*).

Fluid inclusion data from quartz overgrowths show quartz cements were precipitated between 95–125°C meaning formation occurred mostly during the burial diagenesis/mesodiagensis stage (Fig. 16). Assuming an internal source, quartz overgrowths precipitated upon detrital quartz grains after the initial stage of mechanical compaction, where the bulk of a rocks intergranular volume is commonly lost (e.g. Paxton *et al.* 2002). Silica was sourced from the dissolution of early framework grains (predominantly K-feldspar, but also some detrital quartz). Internal silica sources have been attributed to quartz cementation in the Slyne Basin (Schmid *et al.* 2004). Quartz cementation is suggested to be more significant in the ASF simply because the ASF facies contain a greater amount of detrital K-feldspar.

The processes outlined above indicate early diagenetic modification following deposition, typical of red-bed style diagenesis in a semi-arid to arid setting (e.g. Burley *et al.* 1985). Infiltrated detrital clays percolated through the unsaturated zone, transported by groundwater and precipitated within intergranular pore spaces and around grains. Smectite is suggested to have been deposited as a detrital weathering deposit during early eodiagenesis, as is common in semi-arid to arid aeolian and, subordinately, fluvial deposits and within the Triassic. This deposition is therefore suggested to be greater in the aeolian KSF, as suggested also by detrital data (Fig. 16; Table 1; McKinley *et al.* 1999; Weibel and Grobety 1999; Lybrand and Rasmussen 2018; Al-Juboury *et al.* 2020). The transformation of this infiltrated smectite into mixed illite–smectite is suggested by the honey-comb texture, before a final transformation into the protruding pore-bridge illite fibres during progressive burial diagenesis (e.g. Weibel 1999; Stricker *et al.* 2016). The transformation of smectite to illite has been reported to occur below

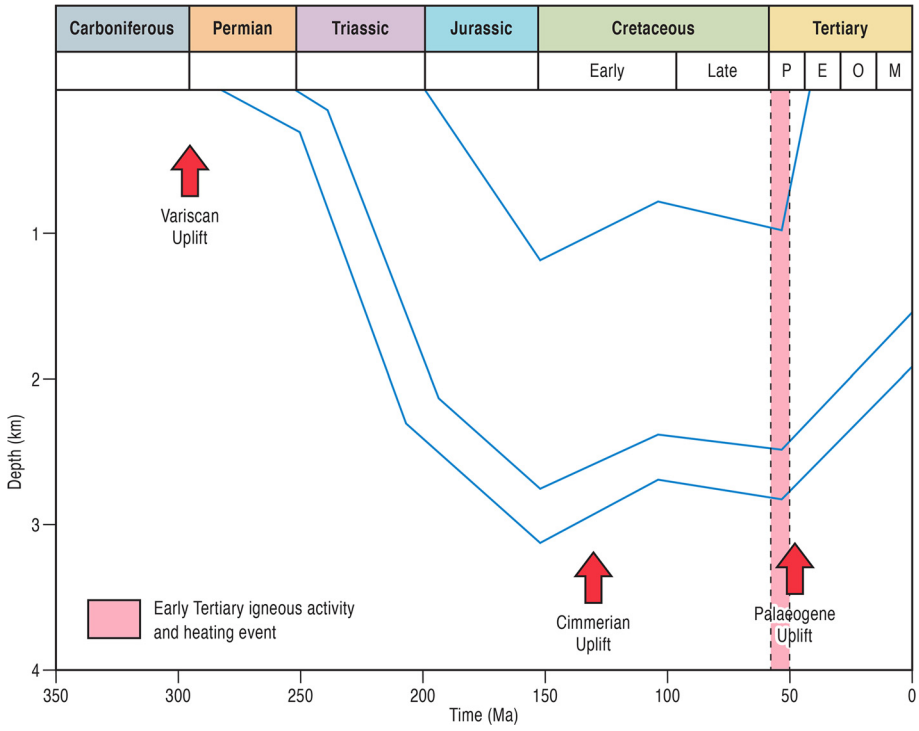

Fig. 15. Reconstructed burial history plot for the Solway and Carlisle Basins, showing important tectonic events.

90°C (Worden and Burley 2003), or may even form at a very low temperature between 20–30°C and depth of 500 m (Buatier *et al.* 1992).

Previous research has suggested that these sediments have been buried to *c.* 3500 m, and a temperature of *c.* 100°C (Newman 1999; Holliday *et al.* 2004). Burial history modelling undertaken in this study has demonstrated a shallower maximum burial depth of *c.* 2800 m and temperature of *c.* 85°C (Fig. 15). At this depth and temperature, it is likely that illite was sourced internally from within the SSG and represents the early alteration products of detrital and/or early diagenetic smectite, as has been suggested in the EISB (e.g. Schmid *et al.* 2004). Other potential potassium sources, such as feldspar dissolution and K-rich circulating pore waters are possible (Thyne *et al.* 2001).

Late stage ferroan dolomite forms microcrystalline rhombs (Fig. 13b) and is heterogeneously distributed throughout the KSF, as seen from local accumulations in the offshore KSF (well 112/19-1). The dolomite stable isotope data displays a variable $\delta^{18}O$ signature, suggesting precipitation over a range of porewater isotope compositions (Fig. 14b). The positive correlation of $\delta^{18}O$ and $\delta^{13}C$ in the dolomite cement is similar to the trend of Naylor *et al.* (1989) for Triassic calcretes (Fig. 14b) and Spötl and Wright (1992) for

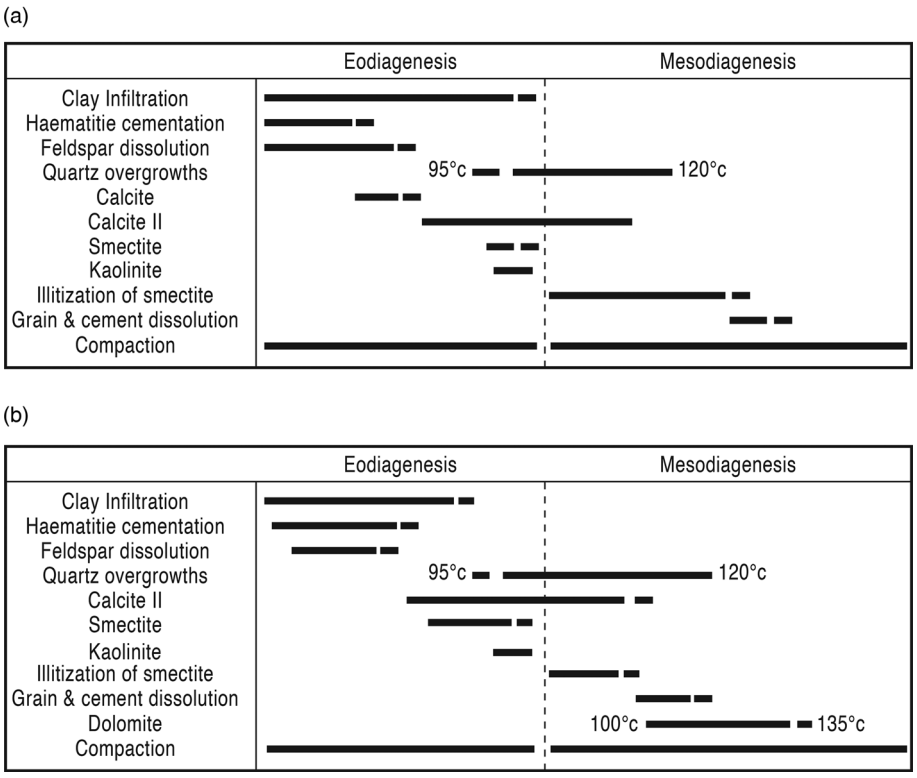

Fig. 16. Paragenetic sequence of the diagenetic minerals in (**a**) the ASF and (**b**) the KSF of the SSG. The temperature for the quartz and dolomite cements were determined from fluid inclusion analysis.

Triassic groundwater dolocretes. Such trends can reflect evaporation of pore waters and a positive shift in the isotopic signature, although it seems unlikely that this has happened for this dolomite burial cement. Fluid inclusion data for dolomite suggest growth occurred between 100 to >135°C placing it firmly in the burial diagenesis realm. The high formation water salinities for dolomite are consistent with precipitation from basinal brines (Warren 2000). The suggested carbonate sources indicate a continued open system during diagenesis (Bjørlykke and Jahren 2012).

Burial history

The precipitation temperatures identified for the quartz and late burial dolomite does not support the burial history modelling in this study (Fig. 15). In order to achieve temperatures of 100°C with an average geothermal gradient, burial depths of >3000 m are required. Such depths are significantly greater than those modelled and either deeper burial has been experienced or elevated heat flow has occurred to explain the fluid inclusion data. Burial compaction fabrics in the ASF and especially the KSF are not compatible with such deep burial, as grains are generally point or long contacts, and pressure solution fabrics are very rare (Fig. 5). The fluid inclusion data is best explained by the pulsed migration of hot fluids through the reservoir sandstones, a suggestion also attributed to similar findings in fields in the EISB (e.g. Greenwood and Habesch 1997). Researchers have proposed that Early Tertiary Igneous activity increased geothermal temperatures and hydrothermal fluid throughout the region, explaining the raised fission-track temperature data found in the EISB, Peel and Solway Basins (Fig. 15) (Greenwood and Habesch 1997; Newman 1999; Quirk *et al.* 1999).

Stable isotope data and fluid inclusion analyses indicate that the later dolomite cements precipitated from evolved saline fluids, compatible with influxes of deep burial brine (e.g. Nguyen *et al.* 2013; Fig. 14). In the EISB, $\delta^{13}C$ data for an equivalent dolomite cement phase indicate that the later cements with a slightly more negative $\delta^{18}O$ signature incorporated greater proportions of ^{12}C-enriched carbon, originating from organic maturation, during burial (Fig. 14; Greenwood and Habesch 1997). This occurrence is not shown in the Solway Basin and through burial history modelling may reflect the late time of oil migration in the EISB, postdating dolomite cement (Newman 1999).

Connection of the Solway Basin to the EISB

Within the EISB, the major northerly flowing 'Budleighensis' fluvial system supplied the vast majority of the basin fill during at least the early stages of Early–Middle Triassic basin evolution (e.g. Meadows and Beach 1993*b*; Tyrrell *et al.* 2007, 2012). Studies using Pb isotopic compositions of detrital K-feldspar grains from the Middle Triassic sandstones of the OSF within the EISB indicate a Variscan uplands source area (Tyrrell *et al.* 2012). Analysis of upstream analogous fluvial deposits from the Wessex Basin further define a dominantly Armorican source from Brittany and Normandy (Newell 2018).

The detailed petrography undertaken in this study, clearly show very similar detrital grain size distributions and burial diagenesis for EISB and Solway Basin (Fig. 6). Furthermore, paleocurrent analysis of channel facies in the ASF reveals a predominantly northward flow direction, similar to the northward paleocurrent direction of the stacked and amalgamated fluvial channels exposed at St Bees Head in West Cumbria, which sits near the boundary between the EISB and Solway Basin (Barnes *et al.* 1994). Based on the remarkable similarity in provenance characteristics between the EISB and the Solway Basin, regional palaeogeographical analysis based on published reconstructions (Newman 1999; Holliday *et al.* 2004) and fluvial palaeocurrent orientation, it seems highly likely that this northward oriented fluvial system flowed from the Cheshire Basin, through the EISB, and continued to flow north into the Solway Basin (Fig. 17a), at least throughout the deposition of the ASF. This contradicts previous studies that have suggested that the Ramsey-Whitehaven Ridge blocked any potential sediment supply from the EISB to the Solway Basin throughout the deposition of the Annan Sandstone (Fig. 1; Newman 1999; Quirk *et al.* 1999). No alternative local source can be invoked to explain such close similarities in provenance between the ASF and SBSF. This reconstruction complies with published accounts of SSG sedimentology in western Britain and suggests that fluvial sediment transport was sourced from areas to the south such as Wales, the English Midlands and Variscan Massifs of SW England (Audley-Charles 1970; Meadows and Beach 1993*b*).

There is, however, a distinct grain size difference between the fluvial and aeolian facies of the Solway Basin and their equivalents in the EISB (Meadows and Beach 1993*a*, *b*). Whilst samples from the SBSF and OSF of the EISB are medium-grained (mean 0.36 mm), the equivalent strata of ASF and KSF from the Solway Basin are very fine-grained and bimodal fine- and medium-grained in nature (mean 0.12 and 0.19 mm/0.28 mm, respectively, Fig. 11). This distinct variation in grain size and the variation in compositional maturity between the sediments of the EISB and those of the Solway Basin can both simply be attributed to fluvial reworking. Detrital grains become finer grained as they are transported further downstream in the fluvial system (Fig. 6), as is documented throughout other British deposits of the SSG (Medici *et al.* 2019).

Relationship to the 'Budleighensis' fluvial system

It has been suggested that the termination of this fluvial drainage system was endorheic and occurred within the distal Solway Basin (e.g. Hounslow and Ruffell 2006). Confining the termination characteristics is of regional importance to the fluvial system.

The Terminal Fan Model, presented by Kelly and Olsen (1993), is proposed to develop where evaporation rates exceed precipitation and runoff rates, establishing a moisture deficit and high levels of infiltration leading to discharge losses. A fluvial distributary zone then forms that is composed of a proximal, medial and distal zone that dissipates entirely downstream into flood basin, playa mudflat or aeolian facies at the basinal zone. Terminal Fans are presented as a feature of drylands or semi-arid to arid climates and systems that experience spatially and temporally fluctuating discharge. Facies trends show a decreasing down-fan grain size and channel body thickness, an increase in siltstone content and a shift to muddy flood basins (Friend 1977; Tunbridge 1984; Kelly and Olsen 1993).

Despite critiques of the Kelly and Olsen (1993) Terminal Fan Model regarding its occurrence in nature, as well as the lack of a distinct sedimentary facies succession (North and Warwick 2007), 'terminal fan' or 'terminal fluvial systems' models, based originally on the Terminal Fan Model, have continued to be adopted (e.g. Masrahy and Mountney 2015). Particularly, such models have been applied within analogous and/or contemporaneous Permo–Triassic dryland river successions to the Solway Basin SSG (Cain and Mountney 2009; McKie and Williams 2009; McKie 2014).

Within the 'terminal fan' or 'terminal fluvial systems' framework, the ASF can be categorized as the distal component of the distributary zone, with smaller channels that largely still dominate, alongside subordinate sheetflood, flood plain fines and aeolian facies (Fig. 18a). Downstream fining, increased clay/mud and silt content compared to the EISB (Fig. 7) and the presence of flood plain and playa type settings which have been described in detail at various localities within the onshore Solway Basin support this (Brookfield 2004, 2008; Holliday *et al.* 2004). At Cove Quarry, stacked channels are still present within the ASF, alongside

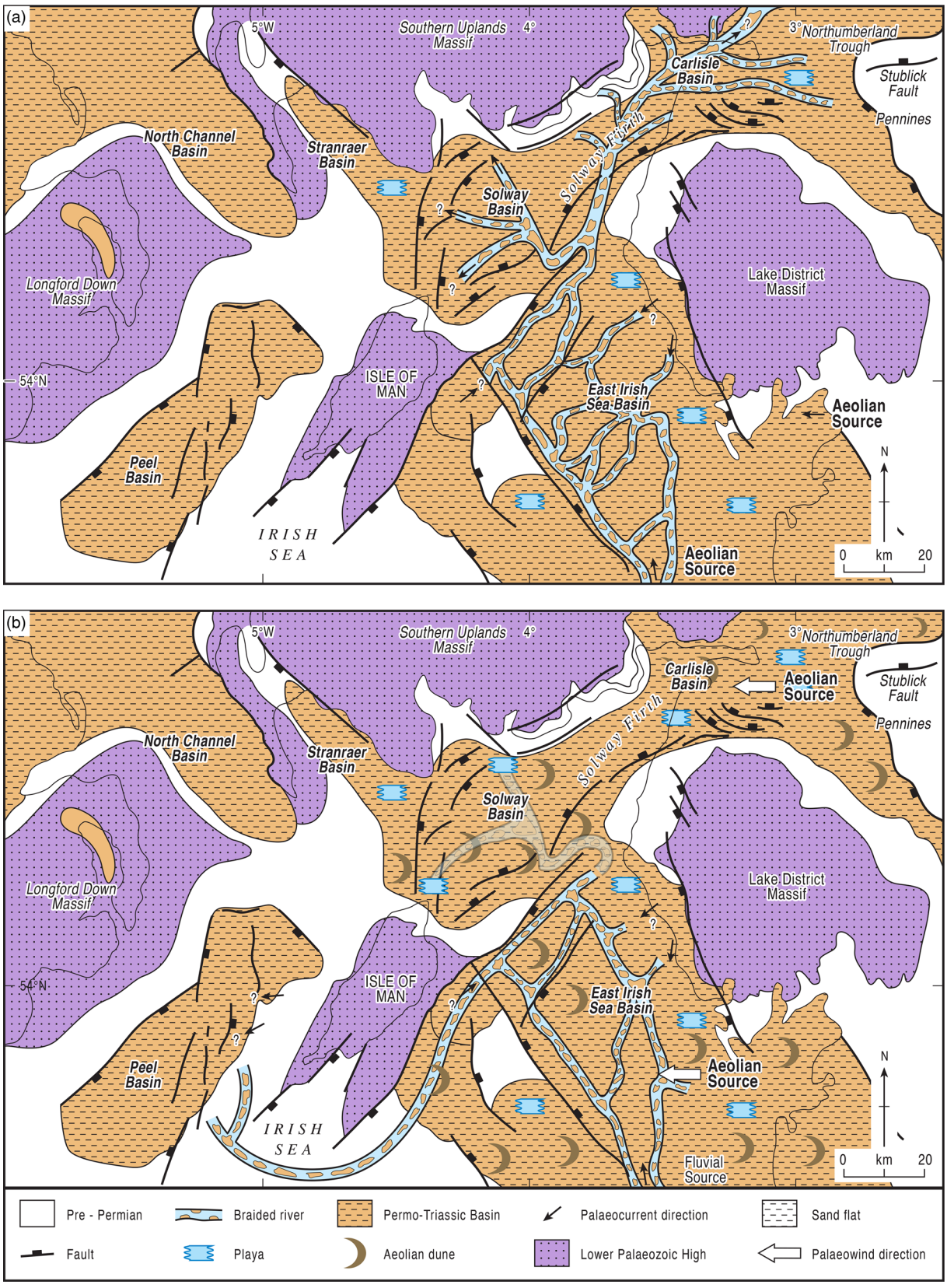

Fig. 17. Schematic palaeogeographies for the EISB and Solway Basins. EISB palaeogeographies modified from Meadows and Beach (1993*a*). (**a**) Deposition of the ASF. Sediment was sourced from the SE via a fluvial system flowing out of the Cheshire Basin, through the EISB and into the Solway Basin, traversing the Ramsey-Whitehaven Ridge. The Solway formed the distal distributary section of this river system with downstream fining and increased clay/mud content compared to the EISB with fluvial channels alongside subordinate sheetflood, flood basin fines, aeolian deposits and playa type settings, (**b**) Deposition of the KSF. The fluvial system diverts away from the Solway Basin and based on well constraints is thought to have diverted towards the Peel basin (Newman 1999). The Solway Basin becomes basinal to the fluvial system, with a lack of discharge leading to predominantly aeolian deposition with episodic flooding events and playa lake sedimentation. A faded channel is featured entering the Solway Basin as wells 112/19-1 and 112/15-1 show channels still periodically returned to the basin, likely during periods of extensive precipitation upon the source. Based on feldspar Pb analysis conducted by Tyrrell *et al.* (2006) and the palaeowind direction, the Shap Granite is identified as a potential additional aeolian source. Further research is required to determine if the palaeo-north Pennines/Durham area served as an aeolian source region during KSF depositional time and supplied sediment for the northern aeolian dune fields, as is suggested for the OSF of west Cumbria (Jones and Ambrose 1994).

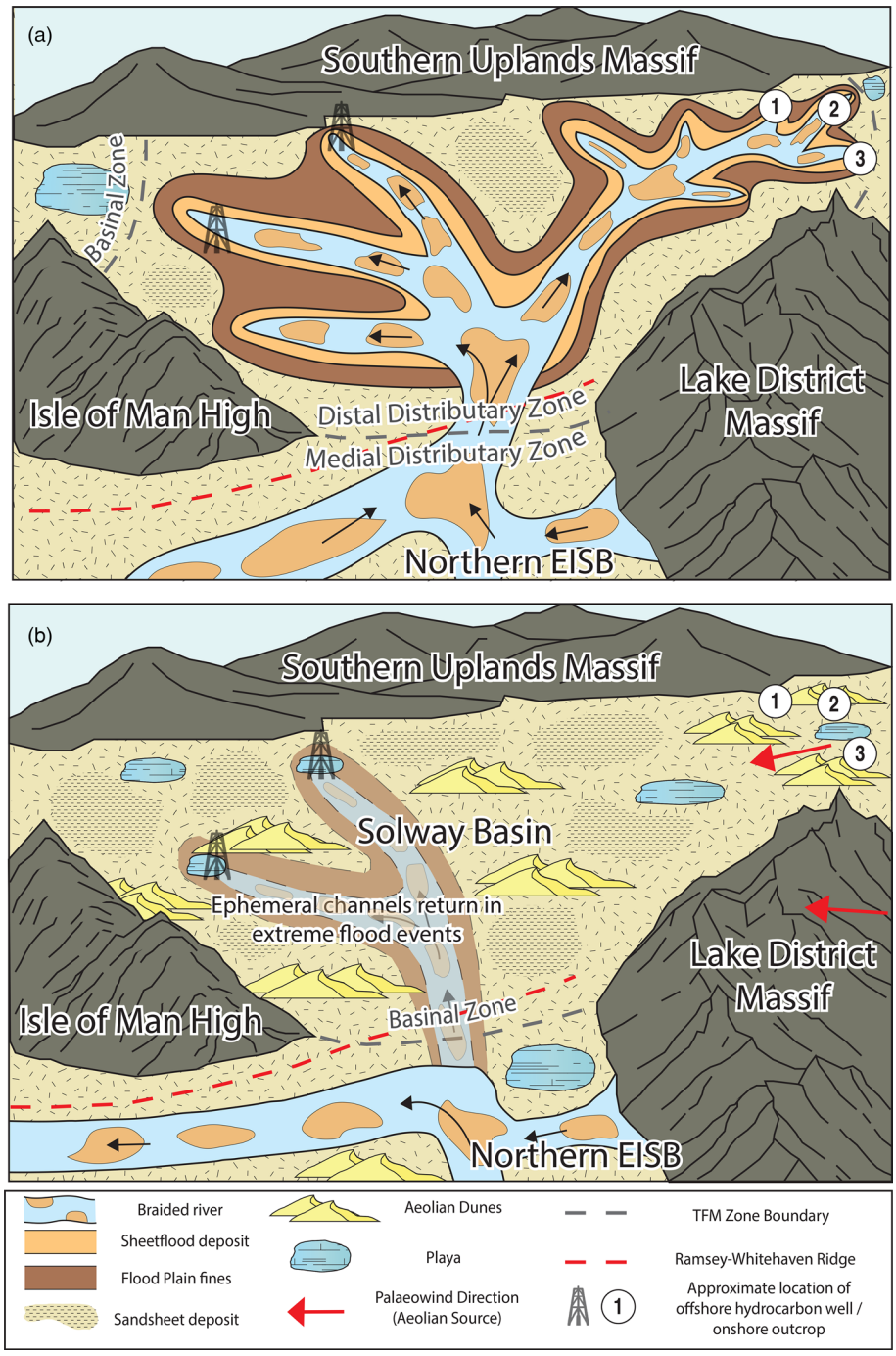

Fig. 18. Facies and Terminal Fan Model (TFM) evolution diagram for the Solway Basin based on Kelly and Olsen (1993) and Cain and Mountney (2009). The approximate locations of the hydrocarbon wells (112/15-1 and 112/19-1) and onshore outcrops (Cove Quarry, Glinger Burn and Bridge Cliff) which are the focus of this study (Fig. 1) are displayed. (**a**) Deposition of the ASF. The EISB represents the medial distributary zone with stacked channel facies. The Solway Basin represents the distal distributary zone with braided channel, sheetflood and floodplain facies. Subordinate sandsheet facies exist between channels. At its margins the basinal zone shows desiccating playa lake facies, (**b**) deposition of the KSF. The Solway Basin has transferred to the basinal zone where aeolian dune, sandsheet and desiccating playa lake facies dominate. Ephemeral channels only return during extreme flood events. The main Budleighensis system diverts westward and the northern EISB sees increased evidence of aeolian and playa lake deposition.

abundant evidence of desiccation and ephemerality which suggests a distal distributary zone rather than a basinal zone, with channels representing periods of increased runoff in the hinterland. The EISB likely represents the medial component of the distributary zone, where its dominant stacked multistorey channel sandstones and interchannel sheetflood facies, as well as minor flood basin mudstones and aeolian components correspond well with the model (Kelly and Olsen 1993; Meadows and Beach 1993*a*; Cain and Mountney 2009). Aeolian reworking of interchannel sandstones is also characteristic of the model and is documented within the EISB (see Mckie and Williams 2009).

The question then remains as to why does the transition from the distal fluvial facies of the ASF to the dominantly aeolian facies of the KSF occur within the Solway Basin whilst fluvial deposition continues within the analogous OSF of the EISB?

The KSF suggests a transition from the distal to basinal zone within the Terminal Fan Model, where dry aeolian facies become dominant once fluvial influence wanes (Kelly and Olsen 1993) (Fig. 18b). Cain and Mountney (2009) propose an analogous transition within the Permian Organ Rock Formation within the Paradox Basin where it is proposed that the terminal fan system transitions to increasingly distal as the fluvial system retreats towards the hinterland and the basinal aeolian dune system advances up the system. The aeolian petrography is characterized by quartz arenites to sub-litharenites which show a reduction in mica, clay and feldspar whilst remaining texturally similar to the fluvial units due to reworking. Petrographically this is equivalent to the transition from the ASF to the KSF (Fig. 6).

The basinal region also characteristically includes flood plains, playa mudstones, evaporites and channels during extreme flood events, as well as aeolian sandstones (Kelly and Olsen 1993). This corresponds well to the blocky mudstone/claystone intervals, evaporite beds and periodic channels sands with wet geophysical characteristics found at the top of the SSG in both offshore Solway Basin wells (Fig. 18b).

One explanation for this transition is that at the time of KSF deposition, the Ramsey–Whitehaven ridge acted as a barrier to the northward oriented fluvial systems that were previously responsible for the deposition of the ASF. Evidence for this is considerable. As previously discussed, wells in the northern parts of the EISB similarly lack significant fluvial deposition (Meadows 2006). This westward shift is explained by regional basin evolution within the East Irish Sea area. Early rifting during the deposition of the SSG within the EISB allowed channels to flow northwards into the Solway Basin. However, as indicated by regional seismic lines (Quirk *et al.* 1999; Floodpage *et al.* 2001), the transition to thermal sag later during the deposition of the SSG re-established the Ramsey–Whitehaven Ridge as a barrier to this previously northward flowing fluvial system. The river then flowed westwards into the Peel Basin (Fig. 17b). Furthermore, dipmeter data in the OSF of the Morecambe Field demonstrates eastwards dipping cross bedding that have been tied to these channels (Cowan 1993). Finally, the increased aeolian deposition within the CSM and OSF within the Sellafield region is thought to be due to tectonism diverting the river system away from the eastern margin (Jones and Ambrose 1994).

Alternatively, a retraction of the 'Budleighensis' fluvial system itself could be the cause of an expansion of the aeolian basinal region within the Solway during the deposition of the KSF. This is supported by the regional upward increase in aeolian deposits and dry facies, as well as evidence of widespread regional evaporitic deposition throughout England and SW Scotland during the later stages of SSG deposition (Ambrose *et al.* 2014). This trend has been proposed to represent a period of increasing aridity in England and a more terminal character of the 'Budleighensis' fluvial system during OSF equivalent deposition (Mckie and Williams 2009; Tyrrell *et al.* 2012; Newell 2018).

Medici *et al.* (2019) quantifies this change, with aeolian facies proportions of 9%, 40% and 47% during ASF-equivalent deposition in the Worcester–Staffordshire Basins, Cheshire Basin and northern onshore EISB-Carlisle Basins, respectively. This changes to 35%, 60% and 100% during the KSF period (see Figure 4 in Medici *et al.* 2019).

Cain and Mountney (2009) propose the distal shift within the Permian Organ Rock Formation was due to an increase in arid conditions and denudation of the primary fluvial source leading to an increase in downstream discharge losses. The Permian Organ Rock Formation is a similar system that was likewise already experiencing strongly seasonal discharge change. Therefore, a regional drying of the 'Budleighensis' fluvial system could similarly be responsible for increased aeolian deposition. Equally, the aeolian shift could be a consequence of a reduction in gradient of the fluvial system (Hounslow and Ruffell 2006). The denudation of Variscan mountain chain is known to have continued throughout the Triassic (Warrington and Ivimey-Cooke 1992).

Decoding the exact cause of the facies change is challenging, with the impact of allocyclic factors difficult to distinguish within continental successions (Péron *et al.* 2005). The 'Budleighensis' fluvial system has already been characterized as sensitive to changes in the water table, with dry periods in the EISB consisting of only small streams, in a geological period prone to significant fluctuations in precipitation (Meadows and Beach 1993*b*; Sellwood and Valdes 2006). Any strengthening of the Pangean monsoon would cause increased seasonality and arid expansion within the continental realm (Parrish 1993). Meanwhile, any potential migration of the humid zone from the Variscan source region would likely significantly affect discharge at the terminal end of the river system (Newell 2018). Periodic return of fluvial facies to the Solway wells during the deposition of the OSF disputes suggestions of a complete separation of the Solway Basin from the EISB due to tectonism along the Ramsey–Whitehaven Ridge.

Aeolian provenance

The provenance for the aeolian KSF is problematical. Given the petrographic similarity between the ASF and KSF, it seems likely that the very fine-grained detrital grain population represents unroofed and reworked material, directly derived from the underlying ASF, as Brookfield (2004, 2008) suggests. Notwithstanding this, the medium-sized grains of the bimodal KSF grain population must be accounted for, as the size of this grain population appears to preclude the possibility of having been derived by wind reworking of the ASF.

Provenance for this period is disputed in literature. Brookfield (2008) states that there is little evidence for present day structural highs, such as the Southern Uplands and the Lake District, affecting Late Paleozoic sedimentation within the sedimentary succession. The Carboniferous palaeo-North Pennines (Askrigg and Alston Blocks) have alternatively been presented as an area of topographic relief during the deposition of the KSF, with the Millstone Grit Group specifically suggested (Meadows and Beach 1993*a*, *b*). Tyrrell *et al.* (2006) disputes this however, citing a radiogenic Pb population found within the Millstone Grit Group that is not present within the EISB. Instead, further Pb analysis of K-feldspars from the EISB (Tyrrell *et al.* 2012) suggests the Shap Granite as a contributory source, which therefore potentially applies to the Solway Basin. However, Tyrrell *et al.* (2012) also accepts an absence of K-feldspar data from the OSF of the Solway Basin. The Pennines/Durham area are suggested to have supplied the majority of sediment to the analogous OSF in the Sellafield area of west Cumbria, an area similar to the Solway Basin in its depositional model and petrography (Jones and Ambrose 1994).

Further research on the provenance of K-feldspars from the Solway Basin is required to determine if the palaeo-north Pennines/Durham area served as an aeolian source region during KSF depositional time and supplied sediment for the northern coarser-grained aeolian dune sediments (Fig. 18). Given that the dominant regional palaeowind was oriented from an East to West direction, this option is feasible (Figs 11 and 17).

Whilst Brookfield's (2004) suggestion of the North Sea region as a potential source area similarly fits the palaeowind direction, the uplifted palaeo-Pennines formed an area of positive relief and likely impeded any wind-blown sediment from the North Sea area (Figs 1 and 18). In addition, the most likely candidate for a source given the palaeo-wind patterns and the stratigraphy of the Central North Sea are the contemporaneous mudstones of the Smith Bank Formation (Goldsmith *et al.* 2003).

Reservoir quality

The sedimentary facies associations in the SSG of the Solway Basin exhibit differing reservoir quality, with the greatest disparity occurring between the flood basin/playa samples of the ASF and those of aeolian dune sandstones in the KSF. The facies control upon reservoir quality is important, but also grain size, sorting and diagenesis (both cementation and compaction) have played a key role within the Solway Basin.

The fine-grained nature of the fluvial sediments within the Solway and Carlisle Basins are due to the basin being situated at the terminal end of the 'Budleighensis' fluvial system. The variable porosities of the ASF (2% to 25%, with a mean of *c.* 13%) are a direct result of the heterogeneous nature of facies distribution because of this distal fluvial location. When ribbon fluvial channel facies and stacked channel facies are deposited, moderate porosity is preserved. A combination of matrix clays, cementation and the fine-grain size however has severely restricted the reservoir potential of the flood basin/playa and sheetflood sequences (Table 1). As a result, the upper ASF, which features fewer interbeds of flood plain

and sheetflood fines has preserved the best reservoir quality of the ASF and a high N:G (77%) in well 112/19-1 (Fig. 8; Table 1).

The main matrix clay within the ASF is illite, which tends to adopt a pore-bridging habit; severely lowering permeabilities and increasing pore tortuosity (Figs 8, 9 and 12d) The widespread occurrence of illite has been well documented within the EISB (Woodward and Curtis 1987; Macchi *et al.* 1990; Meadows and Beach 1993*a*) and in this case, tends to form in box work or honeycomb type textures, severely bridging and infilling intergranular pores. However, illite, by possessing a dominant pore-bridging morphology within the ASF of the Solway Basin, is volumetrically less significant than examples of platy illite documented within the EISB, and its deleterious effect upon reservoir quality is far less.

Porosity loss from cementation has similarly reduced the reservoir quality of the ASF, with both calcite cementation and greater quartz cementation within the ASF compared to the KSF. Calcite cementation is identified as the primary mechanism of porosity loss, constituting up to 13%, with two stages identified (calcite I and II), whilst only minor quantities of the late-stage cement (calcite II) are found within the KSF. Calcite cementation is also tentatively found to be present in greater quantities within the flood basin and subordinately sheetflood facies of the ASF (Table 1).

In the worst affected instances (those where extensive calcite cements combine with illite), both porosities and permeabilities have been reduced to the level where these intervals are effectively non-reservoir, and these facies exhibit a permeability range an order of magnitude lower than the KSF aeolian sandstones (Newman 1999).

Excellent reservoir quality is maintained within the aeolian KSF, where the highest porosity and permeability values are preserved in the aeolian dune facies, where variation away from these higher values in the offshore KSF are found within the fluvial and 'wet' interdune facies (Fig. 9).

Variations away from the mean porosity at Bridge Cliff are largely due to the inherent variations in the quality of aeolian sands in response to differences in grain size and sorting as a result of pinstripe lamination and dune bounding surfaces (see Fig. 3b). Studies of packing parameters have identified that sands composed predominantly of high sphericity grains have lower primary porosities at the time of deposition compared to those grains of low sphericity (e.g. Dickin 1973). High sphericity however in this case has not impeded porosity preservation within the KSF when compared to the less porous ASF, which features less spherical grains, and has therefore not been the determining factor in the porosity preservation of these Formations.

The smectite and mixed layer illite–smectite grain coats abundant within the KSF (Fig. 5b) are suggested to represent a dominant method of porosity preservation. The presence of these detrital grain covers masked potential nucleation sites, preventing later stage growth of cements and crystals upon quartz grain surfaces. This phenomenon, of early infiltrated smectite later forming porosity preserving illite–smectite grain covers has been documented in many studies and is widely regarded as an excellent method of preserving primary intergranular porosity (e.g. Storvoll *et al.* 2002; Ajdukiewicz and Larese 2012). Specifically, Tang *et al.* (2018) reported that aeolian and interdune facies in the Upper Devonian deposits in the North Sea saw increased porosity preservation by this method as they featured greater amounts of mechanically infiltrated smectitic-rich clay bearing water at deposition. This process inhibited quartz cementation in the aeolian deposits and the fluvial deposits, which lacked illite–smectite grain coatings, saw poorer porosity preservation. As the KSF features a greater amount of smectite and this is characteristic of aeolian deposits in semi-arid to arid environments, then this could partially explain the increased quartz cementation and decreased porosity preservation in the fluvial ASF compared with the aeolian KSF (Table 1). It is likely that the present illite grain coatings still played a role in inhibiting quartz cementation within the ASF however the effects of abundant pore-occluding and bridging illite and calcite cementation detracted from much of this.

It has also been recognized that infiltrated clay coatings on framework grains may act as nucleation sites for the precipitation of other authigenic clays (Matlack *et al.* 1989), which aid in the complete coating of detrital framework grains to further prevent quartz precipitation. Although these clays do occlude pore space, the minor degree to which this is the case (<5%), far outweighs the potential porosity which may be lost by late stage authigenic quartz precipitation, up to 12% within fluvial sandstones in the EISB (Meadows and Beach 1993*a*).

It is assumed that the higher porosity, lower number of long grain contacts of the KSF and minimal compaction is due to an early framework stabilizing quartz cement. This accounts for the greater number of grain-to-grain point contacts and corresponding higher porosity compared to the ASF (Fig. 8b). The relatively minor degree to which this early cement has helped to resist compaction in the ASF has meant that 'wet' facies were more susceptible to compaction during early burial (Figs 5 and 8). At the initial critical stage of burial, this early cement phase also helped to resist the effects of compaction, lithifying the sandstones and allowing detrital grains to maintain *c.* 76% 'point' contacts (Fig. 8b). Consequently, pore throats have remained open, pore connectivity is maintained, and primary porosity is preserved.

The presence of this early framework stabilizing quartz cement in the KSF but absence in the ASF may be in part due to the cleaner composition of the aeolian sub-quartz arenite KSF, leading to fewer reactants being available during the onset of diagenesis. Alternatively, the grain contact and compaction differences could be a result of a difference in detrital composition between the ASF and KSF, however considering their remarkably similar composition a stabilizing quartz cement is perhaps more likely (Table 1).

Overall, whilst porosity is variable (14% to 28% and a mean porosity of 21%) in the aeolian KSF, from the samples taken and offshore correlation, the values are equivalent to, or better, than porosities of the equivalent strata in the EISB (Table 1; Figs 8 and 9). The basinal location of the KSF has meant that increased aeolian dune deposition has occurred, which preserve better quality reservoir sands than the mixed fluvial-aeolian sands of the EISB. A consequence of this distal location however is that the playa facies also present significantly reduce porosity and permeability and cause cause lateral anisotropy, as seen with the net:gross difference between wells 112/15-1 and 112/19-1 (Fig. 18b).

Reservoir utility for carbon storage

Hydrocarbon exploration of the Solway Basin was unsuccessful in identifying any prospects (Newman 1999; Floodpage *et al.* 2001). This was due to extensive erosion of the Carboniferous source rock as a result of Variscan Uplift (e.g. Newman 1999), with proven thicknesses of just *c.* 330 and *c.* 74 m in wells 112/15-1 and 112/19-1, respectively. Complete erosion of the Carboniferous Westphalian Group was found in well 112/15-1, with Namurian and Dianantian Group rocks lacking in any source rock lithologies. As a result, the Solway Basin features an excellent reservoir system with a thick MMG caprock that, unlike its analogous EISB counterparts, is uncharged by hydrocarbons (Fig. 19). This presents a possible novel opportunity to explore the use of the Solway Basin for CO_2 storage. As an uncharged reservoir with no history of hydrocarbon (or other commercial) utility the Solway Basin reservoir is classed as a 'saline aquifer'.

Hydrocarbon and CO_2 storage systems are both characterized by the need for a porous and permeable reservoir unit with an overlying

thick and laterally extensive impermeable seal unit. Additional characterization for CO_2 storage reservoirs then must take into accounts the conditions required for successful physical and geochemical trapping of CO_2. For CO_2 storage a structural trap may not be required (e.g. Utsira Formation at Sleipner), just a stratigraphic trapping barrier to halt the migration of an upward migrating CO_2 plume for a short period (<100 years) whilst more permanent trapping mechanisms take effect (Burnside and Naylor 2014). Physical residual/capillary trapping is dependent on pore-scale capillary heterogeneity and has been found to increase storage security significantly and rapidly by immobilizang CO_2 and therefore reducing pressure on the caprock, working at timescales of <100 years (Ajayi *et al.* 2019). Geochemical solubility trapping, which dissolves buoyant supercritical CO_2 into the formation water brine, is dependent on the solubility of CO_2. It is therefore dependent mainly on pressure, temperature and salinity, where solubility increases with increasing depth but decreases with increasing temperature and salinity (Benson and Cole 2008). The timescale for such reactions varies but is likely in the magnitude of hundreds to thousands of years (Burnside and Naylor 2014). Mineral trapping then converts CO_2 into the solid mineral phase, where reactions are dependent on reservoir conditions and the minerals present within the host rock and brine. The process is very advantageous for safe storage but is extremely slow and occurs over thousands to millions of years (Bachu *et al.* 1994).

For successful CO_2 injectivity, the reservoir must be buried to a depth great enough that the temperature and pressure keep the CO_2 in a supercritical phase (>31.1°C and >7.38 MPa), where it possesses a higher density than gaseous CO_2 but still flows as a gas. At regular geothermal gradients this depth is *c.* 800 m depth (Johnson *et al.* 2004). Reservoir depth should be great enough as to not affect groundwater resources and adequately saline (total dissolved solids >10 000 ppm) as to be unsuitable for any other purpose (Benson and Cole 2008; Ajayi *et al.* 2019).

The current paradigm for CO_2 storage site selection is that disused hydrocarbon sites' proven ability to store hydrocarbons will similarly make them suitable for carbon storage with proven trap mechanisms reducing risk (Gammer *et al.* 2011). The presence of infrastructure and a bias of data being available for these regions is also more economical. These factors are inversely the disadvantages of exploiting saline aquifer targets. As such these sites are the primary CO_2 storage targets in Britain despite saline aquifers making up the majority (*c.* 88%) of overall storage potential (ETI 2011). However, disused hydrocarbon sites have inherent disadvantages also. The integrity of legacy abandoned wells within the injection region must be investigated as these may have degraded structural integrity and could pose as sites of potential CO_2 leakage (Ajayi *et al.* 2019). The likely presence of residual hydrocarbon such as natural gas will compete for pore-space with CO_2 and is expected to have significant impacts upon multiphase flow during CO_2 injection and affect residual trapping (Saeedi and Rezaee 2012).

The Solway Basin as a saline aquifer CO_2 storage site has numerous advantages. In this study it has been identified that the reservoir quality is excellent. Porosity and permeability are better than or comparable to the EISB where CO_2 injection is planned by 2025 as part of the Hynet North West Project. This project will target the analogous stratigraphy of depleted gas fields such as Hamilton, where the OSF reservoir target features a mixture of mainly mixed aeolian (dune, sandsheet and sabkha) and stacked fluvial sand facies with subordinate playa margin shale and playa lake facies (ETI 2016; GOV.UK 2021). The reservoir units in the

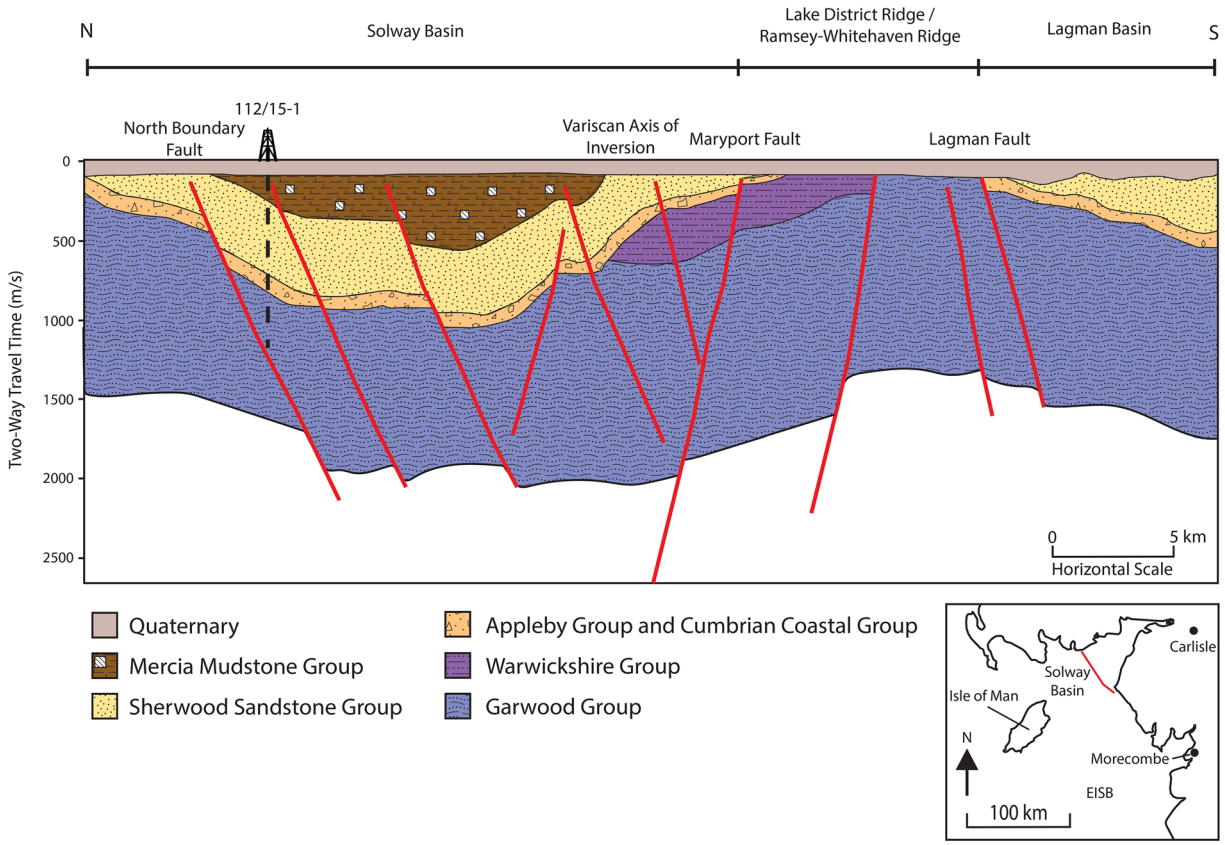

Fig. 19. Illustrative cross-section from a north–south seismic survey across the Solway Basin. Key lithological groups are identified; Quaternary fill, Mercia Mudstone Group (seal/caprock lithology), Sherwood Sandstone Group (reservoir target), (Permian) Appleby Group–Cumbrian Coastal Group and the Carboniferous underburdens, the Warwickshire Group and Garwood Group. Profile corresponds with a combined seismic line from LNX85-13-OM and LNX85-13A-OM, both of which are available from UKOGL. Interpretations are based on Pharaoh *et al.* (2016, 2018).

Solway Basin are also located deeper than the *c.* 800 m TVDSS threshold for storing CO_2 in the supercritical phase, where the primary store KSF is located within the optimum storage depth of 800–1000 m, after which there is no significant benefit of storing CO_2 at greater depths (Ennis-King and Paterson 2002; Gammer *et al.* 2011).

The Solway Basin is classed as an 'open' saline aquifer as no specific stratigraphic/structural traps are identified, unlike 'closed' disused hydrocarbon reservoirs, and therefore CO_2 can migrate laterally without boundaries. As the reservoir generally dips toward the basin centre, buoyancy driven up-dip lateral migration toward the basin margins could risk leakage (Fig. 20). However, as proven by Sleipner, structural confinement is not essential for secure CO_2 storage and updip migration is limited by residual gas trapping and the rate of CO_2 dissolution into formation pore waters, which prevents migration further than a few tens of kilometres (Ennis-King and Paterson 2002). Furthermore, fault-block structural traps have been tested at well sites 112/15-1 and 112/19-1, in addition to trench-collapse structures being found around the perimeter of the basin where the MMG seal is downfaulted against the reservoir unit, which would form barriers to lateral migration out of the basin (Newman 1999; Floodpage *et al.* 2001). A theoretical injection site could include an area around one of the two hydrocarbon wells where the structural traps and collapse-trenches could be utilized, where well 112/15-1 has a greater reservoir and caprock thickness. Alternatively, injection nearer the basin centre features the thickest extent of reservoir and caprock, allowing for greatest storage capacity and security, if lateral migration to the basin margin can be ruled out.

The Solway Basin has good potential for CO_2 trapping. Physical trapping will be extensive due to the thick and very fine grained MMG caprock which has alternating layers of low permeability muds and excellent halite salt seals (Newman 1999). Residual trapping could be extensive due to heterogeneity between dry aeolian sands and wet interdune and playa deposits in the KSF, which could provide baffles and permeability barriers alike to the thin mudstone interbeds within the Utsira Formation in the Sleipner Project which trapped the bulk of the injected CO_2 before it reached the reservoir–seal interface (Chadwick *et al.* 2004). This heterogeneity makes the Solway Basin KSF analogous to the 'wet aeolian deposystem' of the natural CO_2 reservoir Middle Jurassic Entrada Sandstone Formation in Utah (e.g. Newell *et al.* 2019). Solubility trapping potential with the Solway Basin could be restricted by the shallow and low-temperature reservoir conditions and highly saline pore waters. Mineral trapping will be aided by the fine grain-size which will increase reaction rate but has not hindered porosity and permeability, and the abundance of rock lithics and feldspars, both of which serve as reactants for mineral-trapping reactions (Watson *et al.* 2003). Feldspars further provide secondary porosity and permeability generation from dissolution with acidic CO_2-enriched pore waters, as shown by natural CO_2 analogue sites (e.g. Teranaki Basin, New Zealand; O'Neill *et al.* 2020).

As a failed hydrocarbon target, the Solway Basin features very little risk of leakage and/or integrity failure from legacy exploration or production wells which are abundant within the EISB. Furthermore, the lack of hydrocarbon extraction avoids the risks of geomechanical failures of the caprock, jeopardising the structural trapping of CO_2 through the reactivation of faults and induced seismicity because of repressurizing an already depleted reservoir (Ajayi *et al.* 2019). A lack of hydrocarbon charging means there are no disadvantages linked to residual hydrocarbon presence or continued generation expected.

A significant challenge is the lack of proximity to major sources of CO_2 compared with the EISB. The closest large point sources are sporadic industry and power stations between the Cumbrian coast, Carlisle and Dumfries, with further coastal sources around Morcombe Bay, Lancaster and Blackpool (UK Emissions Interactive Map 2022). CO_2 collection from these point sources and subsequent transport to a CO_2 storage hub in the Solway Basin could be established, such as with the Norwegian Longship Project (Northern Lights 2022). Alternatively, the Solway Basin could serve as a further storage facility to the HyNet North West Project, where CO_2 already plans on being sourced by CO_2 shipping (Hynet 2021).

The Solway Basin also faces the issue of a lack of regional understanding and infrastructure due to a lack of previous economic interest, requiring further investment before injection, a problem all saline aquifers face despite their dominance in CO_2 storage potential (Bentham *et al.* 2014). The Solway at least benefits from extensive research conducted on its analogous reservoir and seal units within the hydrocarbon producing EISB. In the short-term, CO_2 storage in the Solway Basin may risk increased expenditure, however initial investment at this point will further our understanding of saline aquifers which will make up the majority of national and international CO_2 storage sites. Additionally, with storage safety such a significant concern to stakeholders and the IPCC (2005) Special Report stating that reservoirs must be 'likely' to retain 99% of stored CO_2 for 1000 years, stable long-term sequestration should be a priority, for which disused hydrocarbon fields may not be suitable.

Conclusions

Detailed petrography and field sedimentology reveal that the extensive 'Budleighensis' river system did exit north into the Solway and Carlisle Basins from the EISB during the deposition of the Lower Triassic Annan Sandstone Formation. This endorheic fluvial system was likely terminal and when applied to the Terminal Fluvial Model of Kelly and Olsen (1993), can be ascribed to the distal distributary zone, with a mix of intermittently ephemeral channels, sheetflood and flood plain facies. During the deposition of the overlying KSF, the Solway Basin and its onshore extension transitioned into the basinal zone, with deposition of aeolian dune and desiccating playa lake facies. Likely this transition was a result of tectonism, centred around the Ramsey-Whitehaven ridge, causing a preferential fluvial migration away from the Solway Basin into the Peel Basin. Evidence of an overprinted regional contraction of the entire fluvial system is additionally speculated.

Porosity, permeability and diagenetic properties were found to be controlled by the distribution of facies, driven by the dynamics of the 'Budleighensis' fluvial system.

Fluvial channels of the ASF preserve moderate porosities (*c.* 13%). Inherent facies heterogeneity in the form of fluvial channel facies but also sheetflood, flood plain/playa facies throughout has resulted in highly variable reservoir quality, especially in fine-grained, clay rich, sheetflood and flood plain/playa facies, which preserve poor reservoir quality. Porosity preservation was hindered by presence of quartz overgrowths, two phases of carbonate cementation and authigenic clays but was aided by the presence of illite which inhibited later stage burial diagenetic cements. Illite, however, decreases permeabilities quite significantly. Where calcite precipitation combines with illite cements, porosities and permeabilities are affected to the point where these intervals are non-reservoir. Deleterious effects of quartz overgrowths have a greater impact in the ASF than the KSF.

Despite the finer grain size of the Solway Basin fill, excellent porosity and permeability is preserved within the aeolian KSF. This is due both to primary sedimentological characteristics such as bimodal grain size distribution and packing, in addition to early diagenetic processes such as early calcite cement and smectite precipitation which created an early framework stabilizing cement and helped to prevent later stage precipitation products occluding pore space.

This paper presents a case for the Solway Basin as a possible saline target for CO_2 storage and for exploring the reservoir properties of distal fluvial or basinal aeolian sequences. The excellent porosity and permeability and lack of legacy well leakage risks present it as credible and stable sub-surface reservoir for long-term sequestration. This potential is jeopardised somewhat by the lack of present infrastructure that will risk increased expenditure. Overall, this work further constrains the carbon storage saline aquifer catalogue of the British Isles, of which carry the greatest storage potential.

Acknowledgements We thank former Centrica Energy for permission to use petrographic data from North and South Morecambe Fields of the East Irish Sea. This paper contains information provided by the Oil and Gas Authority and/or other third parties.

Author contributions **JRM**: conceptualization (lead), data curation (lead), formal analysis (equal), investigation (lead), methodology (equal), resources (supporting), visualization (equal), writing – original draft (lead), writing – review & editing (equal); **SJJ**: conceptualization (supporting), formal analysis (equal), methodology (equal), resources (lead), supervision (lead), visualization (equal), writing – review & editing (equal); **NSM**: conceptualization (supporting), formal analysis (equal), methodology (equal), supervision (supporting), writing – original draft (equal), writing – review & editing (equal); **JGG**: conceptualization (supporting), formal analysis (equal), methodology (equal), supervision (supporting), visualization (equal), writing – review & editing (equal)

Funding This research received no specific grant from any funding agency in the public, commercial, or not-for-profit sectors.

Competing interests The authors declare that they have no known competing financial interests or personal relationships that could have appeared to influence the work reported in this paper.

Data availability The offshore well datasets analysed during the current study are available from the Oil and Gas Authority, through the National Data Repository (https://ndr.ogauthority.co.uk). All other data generated or analysed during this study are included in this published article.

References

Abramoff, M.D., Magelhaes, P.J. and Ram, S.J. 2004. Image processing with ImageJ. *Biophotonics International*, **11**, 36–42.

Ajayi, T., Gomes, J.S. and Bera, A. 2019. A review of CO_2 storage in geological formations emphasizing modeling, monitoring and capacity estimation approaches. *Petroleum Science*, **16**, 1028–1063, https://doi.org/10.1007/s12182-019-0340-8

Ajdukiewicz, J.M. and Larese, R.E. 2012. How clay grain coats inhibit quartz cement and preserve porosity in deeply buried sandstones: Observations and experiments. *AAPG Bulletin*, **96**, 2091–2119, https://doi.org/10.1306/02211211075

Akhurst, M.C., Chadwick, R.A., Holliday, D.W., McCormack, M., McMillan, A.A., Millward, D. and Young, B. 1997. *Geology of the West Cumbria District*. Memoir of the British Geological Survey, Sheets 28, 37 and 47.

Al-Juboury, A.I., Hussain, S.H., McCann, T. and Aghwan, T.A. 2020. Clay mineral diagenesis and red bed colouration: a SEM study of the Gercus Formation (Middle Eocene), northern Iraq. *Geological Journal*, **55**, 7977–7997, https://doi.org/10.1002/gj.3915

Al-Masrahy, M.A. and Mountney, N.P. 2015. A classification scheme for fluvial–aeolian system interaction in desert-margin settings. *Aeolian Research*, **17**, 67–88, https://doi.org/10.1016/j.aeolia.2015.01.010

Ambrose, K., Hough, E., Smith, N.J.P. and Warrington, G. 2014. *Lithostratigraphy of the Sherwood Sandstone Group of England, Wales and South-West Scotland*. British Geological Survey Research Report, **RR/14/01**.

Audley-Charles, M.G. 1970. Triassic palaeogeography of the British Isles. *Quarterly Journal of the Geological Society, London*, **126**, 49–89, https://doi.org/10.1144/gsjgs.126.1.0049

Bachu, S., Gunter, W. D. and Perkins, E. H. 1994. Aquifer disposal of CO2: Hydrodynamic and mineral trapping. *Energy Conversion and Management*, **35**, 269–279, http://doi.org/10.1016/0196-8904(94)90060-4.

Barnes, R.P., Ambrose, K., Holliday, D.W. and Jones, N.S. 1994. Lithostratigraphical subdivision of the Triassic Sherwood sandstone group in west Cumbria. *Proceedings of the Yorkshire Geological Society*, **50**, 51–60, https://doi.org/10.1144/pygs.50.1.51

Benson, S. M. and Cole, D. R. 2008. CO2 sequestration in deep sedimentary formations. *Elements*, **4**, 325–331, https://doi.org/10.2113/gselements.4.5.325

Bentham, M., Mallows, T., Lowndes, J. and Green, A. 2014. CO2 STORrage evaluation database (CO2 Stored). The UK's online storage atlas. *Energy Procedia*, **63**, 5103–5113, https://doi.org/10.1016/j.egypro.2014.11.540

Bjørlykke, K. and Jahren, J. 2012. Open or closed geochemical systems during diagenesis in sedimentary basins: constraints on mass transfer during diagenesis and the prediction of porosity in sandstone and carbonate reservoirs. *AAPG Bulletin*, **96**, 2193–2214, https://doi.org/10.1306/04301211139

Brookfield, M.E. 2004. The enigma of fine-grained alluvial basin fills: the Permo-Triassic (Cumbrian Coastal and Sherwood Sandstone Groups) of the Solway Basin, NW England and SW Scotland. *International Journal of Earth Sciences*, **93**, 282–296, https://doi.org/10.1007/s00531-004-0381-z

Brookfield, M.E. 2008. Palaeoenvironments and palaeotectonics of the arid to hyperarid intracontinental latest Permian- late Triassic Solway basin (U.K.). *Sedimentary Geology*, **210**, 27–47, https://doi.org/10.1016/j.sedgeo.2008.06.003

Buatier, M.D., Peacor, D.R. and O'Neil, J.R. 1992. Smectite-illite transition in Barbados accretionary wedge sediments: TEM and AEM evidence for dissolution/crystallization at low temperature. *Clays and Clay Minerals*, **40**, 65–80, https://doi.org/10.1346/CCMN.1992.0400108

Burley, S.D. 1984. Patterns of sandstone diagenesis in the Sherwood Sandstone Group (Triassic), United Kingdom. *Clay Minerals*, **19**, 403–440, https://doi.org/10.1180/claymin.1984.019.3.11

Burley, S.D., Kantorowicz, J.D. and Waugh, B. 1985. Clastic diagenesis. *Geological Society, London, Special Publications*, **18**, 189–226, https://doi.org/10.1144/GSL.SP.1985.018.01.10

Burnside, N.M. and Naylor, M. 2014. Review and implications of relative permeability of CO_2/brine systems and residual trapping of CO_2. *International Journal of Greenhouse Gas Control*, **23**, 1–11, https://doi.org/10.1016/j.ijggc.2014.01.013

Cain, S.A. and Mountney, N.P. 2009. Spatial and temporal evolution of a terminal fluvial fan system: the Permian Organ Rock Formation, South-east Utah, USA. *Sedimentology*, **56**, 1774–1800, https://doi.org/10.1111/j.1365-3091.2009.01057.x

Cerling, T.E. 1991. Carbon dioxide in the atmosphere: evidence from Cenozoic and Mesozoic paleosols. *American Journal of Science*, **291**, 377–400, https://doi.org/10.2475/ajs.291.4.377

Chadwick, R.A. 1997. *Fault analysis of the Cheshire Basin, NW England*. Geological Society, London, Special Publications, **124**, 297–313, https://doi.org/10.1144/GSL.SP.1997.124.01.18

Chadwick, R.A. and Evans, D.J. 1995. The timing and direction of Permo-Triassic extension in southern Britain. *Geological Society, London, Special Publications*, **91**, 161–192, https://doi.org/10.1144/GSL.SP.1995.091.01.09

Chadwick, R.A., Holliday, D.W., Holloway, S. and Hulbert, A.G. 1995. *The Structure and Evolution of the Northumberland-Solway Basin. Subsurface Memoir of the British Geological Survey*. HMSO, London.

Chadwick, R.A., Jackson, D.I. *et al.* 2001. *Geology of the Isle of Man and Its Offshore Area*. British Geological Survey Research Report, **RR/01/06**.

Chadwick, R.A., Zweigel, P., Gregersen, U., Kirby, G.A., Holloway, S. and Johannessen, P.N. 2004. Geological reservoir characterization of a CO2 storage site: The Utsira Sand, Sleipner, northern North Sea. *Energy*, **29**, 1371–1381, https://doi.org/10.1016/j.energy.2004.03.071

Chandler, M.A., Goggin, D.J. and Lake, L.W. 1989. A mechanical field permeameter for making rapid, non-destructive, permeability measurements. *Journal of Sedimentary Research*, **59**, 613–635, https://doi.org/10.1306/212F9007-2B24-11D7-8648000102C1865D

Colter, V.S. and Bar, K.W. 1975. Recent Developments in the Geology of the Irish Sea and Cheshire Basins'. In: Woodland, A.W. (ed.) *Petroleum and the Continental Shelf of North-West Europe*. Applied Science Publishers, London, **1**, 61–75.

Cowan, G. 1993. Identification and significance of aeolian deposits within the dominantly fluvial Sherwood Sandstone Group of the East Irish Sea Basin UK. *Geological Society, London, Special Publications*, **73**, 231–245, https://doi.org/10.1144/GSL.SP.1993.073.01.14

Dancer, P.N., Kenyon-Roberts, S.M., Baillie, J.M., Meadows, N.S. and Maguire, K. 2005. The Corrib gas field, offshore west of Ireland. *Petroleum Geology: North-West Europe and Global Perspectives – Proceedings of the 6th Petroleum Geology Conference, Geological Society, London*, **6**, 1035–1046, https://doi.org/10.1144/0061035

Dickin, E. 1973. Influence of grain shape and size upon the limiting porosities of sands. STP523-EB Evaluation of Relative Density and its Role in Geotechnical Projects Involving Cohesionless Soils, Los Angeles, CA, 113–120, https://doi.org/10.1520/STP37867S

Ennis-King, J. and Paterson, L. 2002. Engineering aspects of geological sequestration of carbon dioxide. SPE Asia Pacific Oil and Gas Conference and Exhibition. OnePetro, https://doi.org/10.2118/77809-MS

ETI 2011. *UK SAP Final Report*. Carbon Capture and Storage, https://data.ukedc.rl.ac.uk/browse/edc/fossil/co2capture/CCS_SAP/Reports [last accessed 19 March 2021].

ETI & Pale Blue Dot 2016. A Summary of Results from the Strategic UK CO_2 Storage Appraisal Project. Progressing Development of the UK's Strategic Carbon Dioxide Storage Resource, 1–46, https://www.eti.co.uk/programmes/carbon-capture-storage/strategic-uk-ccs-storage-appraisal [last accessed 16 March 2021].

Evans, D.J., Rees, J.G. and Holloway, S. 1993. The Permian to Jurassic stratigraphy and structural evolution of the central Cheshire Basin. *Journal of*

the Geological Society, **150**, 857–870, https://doi.org/10.1144/gsjgs.150.5.0857

Floodpage, J., Newman, P. and White, J. 2001. Hydrocarbon prospectivity in the Irish Sea area: insights from recent exploration of the Central Irish Sea, Peel and Solway basins. *Geological Society, London, Special Publications*, **188**, 107–134, https://doi.org/10.1144/GSL.SP.2001.188.01.06

Friend, P.F. 1977. Distinctive features of some ancient river systems. In: Miall, A.D. (ed.) *Fluvial Sedimentology. Memoir*, **5**, 531–542.

Gammer, D., Smith, G. and Green, A. 2011. *Energy Technology Institute*. Society of Petroleum Engineers. SPE Number 148426, 1045–1058.

Goldsmith, P.J., Hudson, G. and Van Veen, P. 2003. Triassic. *The Millennium Atlas: Petroleum Geology of the Central and Northern North Sea*. *Geological Society, London*, 105–107.

Goldstein, R.H. 2001. Fluid inclusions in sedimentary and diagenetic systems. *Lithos*, **55**, 159–193, https://doi.org/10.1016/S0024-4937(00)00044-X

Goldstein, R.H. and Reynolds, T.J. 1994. *Fluid Inclusion Microthermometry*. SEPM.

GOV.UK 2021. October 2021 update: track-1 clusters confirmed, https://www.gov.uk/government/publications/cluster-sequencing-for-carbon-capture-usage-and-storage-ccus-deployment-phase-1-expressions-of-interest/october-2021-update-track-1-clusters-confirmed [last accessed 25 November 2021].

Greenwood, P.J. and Habesch, S.M. 1997. Diagenesis of the Sherwood Sandstone Group in the southern East Irish Sea Basin (Blocks 110/13, 110/14 and 110/15): constraints from preliminary isotopic and fluid inclusion studies. *Petroleum Geology of the Irish Sea and Adjacent Areas, Geological Society Special Publications*, **124**, 353–371, https://doi.org/10.1144/GSL.SP.1997.124.01.21

Grove, C. and Jerram, D.A. 2011. jPOR: an ImageJ macro to quantify total optical porosity from blue-stained thin sections. *Computers & Geosciences*, **37**, 1850–1859, https://doi.org/10.1016/j.cageo.2011.03.002

Holliday, D.W., Warrington, G., Brookfield, M.E., McMillan, A.A. and Holloway, S. 2001. Permo-Triassic rocks in boreholes in the Annan-Canonbie area, Dumfries and Galloway, southern Scotland. *Scottish Journal of Geology*, **37**, 97–113, https://doi.org/10.1144/sjg37020097

Holliday, D.W., Holloway, S., McMillan, A.A., Jones, N.S., Warrington, G. and Akhurst, M.C. 2004. The evolution of the Carlisle Basin, NW England and SW Scotland. *Proceedings of the Yorkshire Geological Society*, **55**, 1–19, https://doi.org/10.1144/pygs.55.1.1

Hounslow, M.W. and Ruffell, A.H. 2006. Triassic: seasonal rivers, dusty deserts and saline lakes. *The Geology of England and Wales*. *The Geological Society, London*, 295–324, https://doi.org/10.1144/GOEWP.13

Houseknecht, D.W. 1987. Assessing the relative importance of compaction processes and cementation to reduction of porosity in sandstones. *AAPG Bulletin*, **71**, 633–642, https://doi.org/10.1306/9488787F-1704-11D7-8645000102C1865D

Hynet 2021. *HyNet North West*, https://hynet.co.uk [last accessed 25 November 2021].

IPCC 2005. Metz, B., Davidson, O., Coninck, H., Loos, M. and Meyer, L. (eds). *Special Report on Carbon Dioxide Capture and Storage*. Cambridge University Press, UK, 431.

Jackson, D.I. and Johnson, H. 1996. *Lithostratigraphic Nomenclature of the Triassic, Permian and Carboniferous of the UK Offshore East Irish Sea Basin*. British Geological Survey.

Jackson, D.I. and Mulholland, P. 1993. Tectonic and stratigraphic aspects of the East Irish Sea Basin and adjacent areas: contrasts in their post-Carboniferous structural styles. *Petroleum Geology of Northwest Europe: Proceedings of the 4th Conference. The Geological Society, London*, **4**, 791–808, https://doi.org/10.1144/0040791

Jackson, D.I., Mulholland, P., Jones, S.M. and Warrington, G. 1987. The Geological framework of the East Irish Sea Basin. *In*: Brooks, J. and Glennie, K. (eds) *Petroleum Geology of North West Europe, Graham and Trotman*, London, pp. 191–204.

Jackson, D.I., Jackson, A.A., Evans, D., Wingfield, R.T.R., Barnes, R.P. and Arthur, M.J. 1995. *The Geology of the Irish Sea*. British Geological Survey United Kingdom Offshore Regional Report. HMSO, London.

Johnson, J.W., Nitao, J.J. and Knauss, K.G. 2004. Reactive transport modelling of CO_2 storage in saline aquifers to elucidate fundamental processes, trapping mechanisms and sequestration partitioning. *Geological Society, London, Special Publications*, **233**, 107–128, https://doi.org/10.1144/GSL.SP.2004.233.01.08

Jones, N.S. and Ambrose, K. 1994. Triassic sandy braidplain and aeolian sedimentation in the Sherwood Sandstone Group of the Sellafield area, west Cumbria. *Proceedings of the Yorkshire Geological Society*, **50**, 61–76, https://doi.org/10.1144/pygs.50.1.61

Katsube, T.J., Bloch, J. and Cox, W.C. 1999*a*. The effect of diagenetic alteration on shale pore-structure and its implications for abnormal pressures and geophysical signatures. Overpressure in Petroleum Exploration: Proceedings of the Workshop: Bulletin Centre Recherche Elf Exploration and Production Memoir, Pau, France, **22**, 4954.

Katsube, T.J., Dallimore, S.R., Uchida, T., Jenner, K.A., Collett, T.S. and Connell, S. 1999*b*. Petrophysical environment of sediments hosting gas-hydrate, JAPEX/JNOC/GSC Mallik 2L–38 gas hydrate research well. *Geological Survey of Canada Bulletin*, **544**, 109124.

Kelly, S.B. and Olsen, H. 1993. Terminal fans – a review with reference to Devonian examples. *Sedimentary Geology*, **85**, 339–374, https://doi.org/10.1016/0037-0738(93)90092-J

Kutzbach, J.E. and Gallimore, R.G. 1989. Pangean climates: megamonsoons of the megacontinent. *Journal of Geophysical Research*, **94**, 3341–3357, https://doi.org/10.1029/JD094iD03p03341

Lybrand, R.A. and Rasmussen, C. 2018. Climate, topography, and dust influences on the mineral and geochemical evolution of granitic soils in southern Arizona. *Geoderma*, **314**, 245–261, https://doi.org/10.1016/j.geoderma.2017.10.042

Macchi, L., Curtis, C.D., Levison, A., Woodward, K. and Hughes, C.R. 1990. Chemistry, morphology, and distribution of illites from Morecambe Gas Field, Irish Sea, offshore United Kingdom. *AAPG Bulletin*, **74**, 296–308, https://doi.org/10.1306/0C9B22D1-1710-11D7-8645000102C1865D

Manspeizer, W. 1988. Triassic-Jurassic rifting and the opening of the Atlantic: an overview. *Triassic-Jurassic Rifting; Continental Breakup, and the Origin of the Atlantic Ocean and Passive Margins*. Elsevier, New YorkF, 41–79, https://doi.org/10.1016/B978-0-444-42903-2.50008-7

Matlack, K.S., Houseknecht, D.W. and Applin, K. 1989. Emplacements of clay into sand by infiltration. *Journal of Sedimentary Petrology*, **59**, 77–87, https://doi.org/10.1306/212F8F21-2B24-11D7-8648000102C1865D

McKie, T. 2014. Climatic and tectonic controls on Triassic dryland terminal fluvial system architecture, central North Sea. *International Association of Sedimentologists Special Publications*, **46**, 19–57, https://doi.org/10.1002/9781118920435.ch2

McKie, T. and Williams, B. 2009. Triassic palaeogeography and fluvial dispersal across the northwest European Basins. *Geological Journal*, **44**, 711–741, https://doi.org/10.1002/gj.1201

McKinley, J.M., Worden, R.H. and Ruffell, A.H. 1999. Smectite in sandstones: a review of the controls on occurrence and behaviour during diagenesis. *Clay mineral cements in sandstones*, pp. 109–128, https://doi.org/10.1002/9781444304336.ch5

Meadows, N.S. 2006. The correlation and sequence architecture of the Ormskirk sandstone formation in the Triassic Sherwood sandstone group of the East Irish Sea Basin, NW England. *Geological Journal*, **41**, 93–122, https://doi.org/10.1002/gj.1034

Meadows, N.S. and Beach, A. 1993*a*. Controls on reservoir quality in the Triassic Sherwood Sandstone of the Irish Sea. *Geological Society, London, Petroleum Geology Conference series*, **4**, 823–833, https://doi.org/10.1144/0040823

Meadows, N.S. and Beach, A. 1993*b*. Structural and climatic controls on facies distribution in a mixed fluvial and aeolian reservoir: the Triassic Sherwood Sandstone in the Irish Sea. *Geological Society, London, Special Publication*, **73**, 247–264, https://doi.org/10.1144/GSL.SP.1993.073.01.15

Medici, G., West, L.J. and Mountney, N.P. 2019. Sedimentary flow heterogeneities in the Triassic U.K. Sherwood Sandstone Group: insights for hydrocarbon exploration. *Geological Journal*, **54**, 1361–1378, https://doi.org/10.1002/gj.3233

Morad, S., de Ros, L.F., Nystuen, J.P. and Bergan, M. 1998. Carbonate diagenesis and porosity evolution in sheet-flood sandstones: evidence from the middle and lower lunde members (Triassic) in the Snorre Field, Norwegian North Sea. *Special Publication International Association of Sedimentologists*, **26**, 53–85, https://doi.org/10.1002/9781444304893.ch3

Mountney, N.P. and Thompson, D.B. 2002. Stratigraphic evolution and preservation of aeolian dune and damp/wet interdune strata: an example from the Triassic Helsby Sandstone Formation, Cheshire Basin, UK. *Sedimentology*, **49**, 805–833, https://doi.org/10.1046/j.1365-3091.2002.00472.x

Naylor, H., Turner, P., Vaughan, D.J. and Fallick, A.E. 1989. The Cherty Rock, Elgin: a petrographic and isotopic study of a Permo-Triassic calcrete. *Geological Journal*, **24**, 205–221, https://doi.org/10.1002/gj.3350240305

Newell, A.J. 2018. Rifts, rivers and climate recovery: a new model for the Triassic of England. *Proceedings of the Geologists' Association*, **129**, 352–371, https://doi.org/10.1016/j.pgeola.2017.04.001

Newell, A.J., Pourmalek, A., *et al.* 2019. The importance of lithofacies control on fluid migration in heterogeneous aeolian formations for geological CO_2 storage: Lessons from observational evidence and modelling of bleached palaeoreservoirs at Salt Wash Graben, Utah. *International Journal of Greenhouse Gas Control*, **91**, 102841, https://doi.org/10.1016/j.ijggc.2019.102841

Newman, P.J. 1999. The geology and hydrocarbon potential of the Peel and Solway Basins, East Irish Sea. *Journal of Petroleum Geology*, **22**, 305–324, https://doi.org/10.1111/j.1747-5457.1999.tb00989.x

Nguyen, B.T.T., Jones, S.J., Goulty, N.R., Middleton, A.J., Grant, N., Ferguson, A. and Bowen, L. 2013. The role of fluid pressure and diagenetic cements for porosity preservation in Triassic fluvial reservoirs of the Central Graben, North Sea. *AAPG Bulletin*, **97**, 1273–1302, https://doi.org/10.1306/01151311163

North, C.P. and Warwick, G.L. 2007. Fluvial fans: myths, misconceptions, and the end of the terminal-fan model. *Journal of Sedimentary Research*, **77**, 693–701, https://doi.org/10.2110/jsr.2007.072

Northern Lights. 2022. https://northernlightsccs.com [Accessed 3 Jan 2022].

O'Neill, S. R., Jones, S. J. and Kamp, P. J. J. 2020. Diagenesis and burial history modeling of heterogeneous marginal marine to shoreface Paleocene glauconitic sandstones, Taranaki Basin, New Zealand. *Journal of Sedimentary Research*, **90**, 651–668, https://doi.org/10.2110/jsr.2020.34

Parrish, J.T. 1993. Climate of the supercontinent Pangea. *The Journal of Geology*, **101**, 215–233, https://doi.org/10.1086/648217

Paxton, S.T., Szabo, J.O., Ajdukiewicz, J.M. and Klimentidis, R.E. 2002. Construction of an intergranular volume compaction curve for evaluating and predicting compaction and porosity loss in rigid-grain sandstone reservoirs. *AAPG Bulletin*, **86**, 2047–2067, https://doi.org/10.1306/61EEDDFA-173E-11D7-8645000102C1865D

Péron, S., Bourquin, S., Fluteau, F. and Guillocheau, F. 2005. Paleoenvironment reconstructions and climate simulations of the Early Triassic: impact of the water and sediment supply on the preservation of fluvial systems. *Geodinamica Acta*, **18**, 431–446, https://doi.org/10.3166/ga.18.431-446

Pharaoh, T.C., Kirk, K. *et al.* 2016. *Seismic Interpretation and Generation of Depth Surfaces for Late Palaeozoic Strata in the Irish Sea Region*. British Geological Survey Commissioned Report, **CR/16/041**, 64, http://nora.nerc.ac.uk/id/eprint/516786

Pharaoh, T.C., Gent, C.M.A., *et al.* 2018. An overlooked play? Structure, stratigraphy and hydrocarbon prospectivity of the Carboniferous in the East Irish Sea-North Channel basin complex. *Geological Society Special Publication*, **471**, 281–316, https://doi.org/10.1144/SP471.7

Preto, N., Kustsatscherc, E. and Wignall, P.B. 2010. Triassic climates - state of the art and perspectives. *Palaeogeography, Palaeoclimatology, Palaeoecology*, **290**, 1–10, https://doi.org/10.1016/j.palaeo.2010.03.015

Quirk, D.G. and Kimbell, G.S. 1997. Structural evolution of the Isle of Man and central part of the Irish Sea. *Petroleum Geology of the Irish Sea and Adjacent Areas. Geological Society, London, Special Publications*, **124**, 135–159, https://doi.org/10.1144/GSL.SP.1997.124.01.09

Quirk, F.G., Roy, S., Knott, I., Redfern, J. and Hill, L. 1999. Petroleum Geology and future hydrocarbon potential of the Irish Sea. *Journal of Petroleum Geology*, **22**, 243–260, https://doi.org/10.1111/j.1747-5457.1999.tb00986.x

Rowley, E. and White, N. 1998. Inverse modeling of extension and denudation in the East Irish Sea and surrounding areas. *Earth and Planetary Science Letters*, **161**, 57–71, https://doi.org/10.1016/S0012-821X(98)00137-X

Saeedi, A. and Rezaee, R. 2012. Effect of residual natural gas saturation on multiphase flow behaviour during CO2 geo-sequestration in depleted natural gas reservoirs. *Journal of Petroleum Science and Engineering*, **82**, 17–26, https://doi.org/10.1016/j.petrol.2011.12.012

Schmid, S., Worden, R.H. and Fisher, Q.J. 2004. Diagenesis and reservoir quality of the Sherwood Sandstone (Triassic), Corrib Field, Slyne Basin, west of Ireland. *Marine and Petroleum Geology*, **21**, 299–315, https://doi.org/10.1016/j.marpetgeo.2003.11.015

Sellwood, B.W. and Valdes, P.J. 2006. Mesozoic climates: General circulation models and the rock record. *Sedimentary Geology*, **190**, 269–287, https://doi.org/10.1016/j.sedgeo.2006.05.013

Spötl, C. and Wright, V.P. 1992. Groundwater dolocretes from the Upper Triassic of the Paris Basin, France: a case study of an arid, continental diagenetic facies. *Sedimentology*, **39**, 1119–1136, https://doi.org/10.1111/j.1365-3091.1992.tb02000.x

Storvoll, V., Bjørlykke, K., Karlsen, D. and Saigal, G. 2002. Porosity preservation in reservoir sandstones due to grain-coating illite: a study of the Jurassic Garn Formation from the Kristin and Lavrans fields, offshore Mid-Norway. *Marine and Petroleum Geology*, **19**, 767–781, https://doi.org/10.1016/S0264-8172(02)00035-1

Stricker, S., Jones, S.J. and Grant, N.T. 2016. Importance of vertical effective stress for reservoir quality in the Skagerrak Formation, Central Graben, North Sea. *Marine and Petroleum Geology*, **78**, 895–909, https://doi.org/10.1016/j.marpetgeo.2016.03.001

Strong, G.E. 1993. Diagenesis of Triassic Sherwood Sandstone Group rocks, Preston, Lancashire, U.K.: a possible evaporitic cement precursor to secondary porosity? *Geological Society Special Publication*, **73**, 279–289, https://doi.org/10.1144/GSL.SP.1993.073.01.17

Szulc, J. 1999. Anisian–Carnian evolution of the Germanic basin and its eustatic, tectonic and climatic controls. *Epicontinental Triassic. Zentralblatt fur Geologie und Palaeontologie, Stuttgart*, **7–8**, 813–852.

Tang, L., Gluyas, J. and Jones, S. 2018. Porosity preservation due to grain coating illite/smectite: evidence from Buchan Formation (Upper Devonian) of the Ardmore Field, UK North Sea. *Proceedings of the Geologists' Association*, **129**, 202–214, https://doi.org/10.1016/j.pgeola.2018.03.001

Thyne, G., Boudreau, B.P., Ramm, M. and Elin Midtbø, R. 2001. Simulation of potassium feldspar dissolution and illitization in the Statfjord Formation, North Sea. *AAPG Bulletin*, **85**, 621–635, https://doi.org/10.1306/8626C965-173B-11D7-8645000102C1865D

Tunbridge, I.P. 1984. Facies model for a sandy ephemeral stream and clay playa complex; the Middle Devonian Trentishoe Formation of North Devon, U.K. *Sedimentology*, **31**, 697–715, https://doi.org/10.1111/j.1365-3091.1984.tb01231.x

Tyrrell, S., Haughton, P.D.W., Daly, J.S., Kokfelt, T.F. and Gagnevin, D. 2006. The use of the common Pb isotope composition of detrital K-feldspar grains as a provenance tool and its application to Upper Carboniferous paleodrainage, northern England. *Journal of Sedimentary Research*, **76**, 324–345, https://doi.org/10.2110/jsr.2006.023

Tyrrell, S., Haughton, P.D.W. and Daly, J.S. 2007. Drainage re-organization during break-up of Pangea revealed by in-situ Pb isotopic analysis of detrital K-feldspar. *Geology*, **35**, 971–974, https://doi.org/10.1130/G4123A.1

Tyrrell, S., Haughton, P.D.W., Sounders, A.K., Daly, J.S. and Shannon, P.M. 2012. Large-scale, linked drainage systems in the NW European Triassic: insights from the Pb isotopic composition of detrital K-feldspar. *Journal of the Geological Society*, **169**, 279–295, https://doi.org/10.1144/0016-76492011-104

UK Emissions Interactive Map. 2022. https://naei.beis.gov.uk/emissionsapp/ [Accessed 3 Jan 2022].

Walker, T.R., Waugh, B. and Grone, A.J. 1978. Diagenesis in first-cycle desert alluvium of Cenozoic age, southwestern United States and northwestern Mexico. *Geological Society of America Bulletin*, **89**, 19–32, https://doi.org/10.1130/0016-7606(1978)89<19:DIFDAO>2.0.CO;2

Warren, J. 2000. Dolomite: occurrence, evolution and economically important associations. *Earth Science Reviews*, **52**, 1–81, https://doi.org/10.1016/S0012-8252(00)00022-2

Warrington, G. and Ivimey-Cooke, H.C. 1992. Triassic. *Atlas of Palaeogeography and Lithofacies*. *Geological Society, London, Memoirs*, **13**, 97–106, https://doi.org/10.1144/GSL.MEM.1992.013.01.11

Watson, N.M., Zwingmann, N., Lemon, N.M. and Tingate, P.R. 2003. Onshore Otway Basin carbon dioxide accumulations: CO2-induced diagenesis in natural analogues for underground storage of greenhouse gas. *The APPEA Journal*, **43**, 637–653, https://doi.org/10.1071/AJ02036

Weibel, R. and Grobety, B. 1999. Pseudomorphous transformation of goethite needles into hematite in sediments of the Triassic Skagerrak Formation, Denmark. *Clay Minerals*, **34**, 657–660, https://doi.org/10.1180/000985599546415

Wills, L.J. 1951. *A Palaeogeographical Atlas of the British Isles and Adjacent Parts of Europe*. Blackie.

Wilson, A.A. 1990. The Mercia Mudstone Group (Trias) of the East Irish Sea Basin. *Proceedings of the Yorkshire Geological Society*, **48**, 1–22, https://doi.org/10.1144/pygs.48.1.1

Woodward, K. and Curtis, C.D. 1987. Predictive modelling of the distribution of production constraining illites - Morecambe Gas Field, Irish Sea, Offshore UK. *In*: Brooks, J. and Glennie, K. (eds) *Petroleum Geology of North West Europe*. Graham & Trotman, London, pp. 205–215.

Worden, R. and Burley, S. 2003. Sandstone diagenesis: the evolution of sand to stone. *In*: *Sandstone Diagenesis*. Blackwell Publishing Ltd, 1–44, https://doi.org/10.1002/9781444304459.ch